RESEARCH ARTICLE



On the rise: using reentrants to extract magma ascent rates in the Bandelier Tuff caldera complex, New Mexico, USA

Megan A. Saalfeld¹ · M. L. Myers¹ · R. deGraffenried² · T. Shea² · C. M. Waelkens³

Received: 17 June 2021 / Accepted: 14 November 2021
© International Association of Volcanology & Chemistry of the Earth's Interior 2021

Abstract

The Bandelier Tuff is the result of two subsequent caldera-forming eruptions of similar volume and composition which produced the Otowi (1.61 Ma) and Tshirege (1.26 Ma) members. Their remarkably similar characteristics and shared caldera boundaries provides a unique platform to investigate whether magma ascent is affected by the presence of a preexisting caldera boundary. Here, we present decompression rates for discrete layers within the initial plinian phase of each member by modeling volatile gradients (H₂O, CO₂ absent) in quartz-hosted reentrants (unsealed melt inclusions). Successful best-fit 1D diffusion models for the lower (n = 4/9) and upper (n = 11/13) units resulted in average decompression rates of 0.041 MPa/s and 0.026 MPa/s, respectively. Strong overlap between rates extracted from the two eruptions suggests there was no significant change in ascent dynamics. However, the older Otowi member contains a larger number of reentrants that cannot be modeled adequately, suggesting a more complicated path than can be reconstructed with our constant decompression approach. In contrast, reentrants from the Tshirege can be readily modeled from storage depths, an observation that suggests conduit formation was more efficient in the second eruption. To further evaluate the robustness of these extracted rates, we then applied a 2D diffusion model, which considers various reentrant geometries; surprisingly, we find little alteration to 1D-derived rates. By contrast, incorporating the uncertainty in Bandelier temperature (~130 °C) shifts rates by 340–440%. However, we argue that the largest source of variation from decompression rates extracted from reentrants lies in the extreme range preserved within each fall deposit, each spanning three orders of magnitude, suggesting extreme conduit dynamic shifts, and emphasizing that petrologic-based ascent rates may vary widely, even within a single-sampled layer. Finally, the lack of detectable CO₂ concentrations in measured profiles is at odds with the amounts detected in sealed melt inclusions (<200 ppm), an observation that has been made in other silicic systems (e.g., Bishop, USA; Oruanui, NZ; Santorini, GR). We propose two mechanisms to remove CO₂ from the system prior to eruption: (1) additional crystallization drove CO₂ into the fluid phase prior to ascent or (2) reentrants reset to a CO₂ free environment due to a small, initial pre-eruptive pressure decrease. Both scenarios have important implications for the pre-eruptive state of the magma body.

Keywords Reentrant · Diffusion · Decompression rate · Magma ascent

Editorial responsibility: T. P. Fischer

Megan A. Saalfeld megansaalfeld@montana.edu

Published online: 08 December 2021

- Department of Earth Sciences, Montana State University, Bozeman, MT 59715, USA
- Department of Earth Sciences, University of Hawai'I at Mānoa, Honolulu, HI 96822, USA
- Department of Earth & Planetary Sciences, McGill University, Montreal, Canada

Introduction

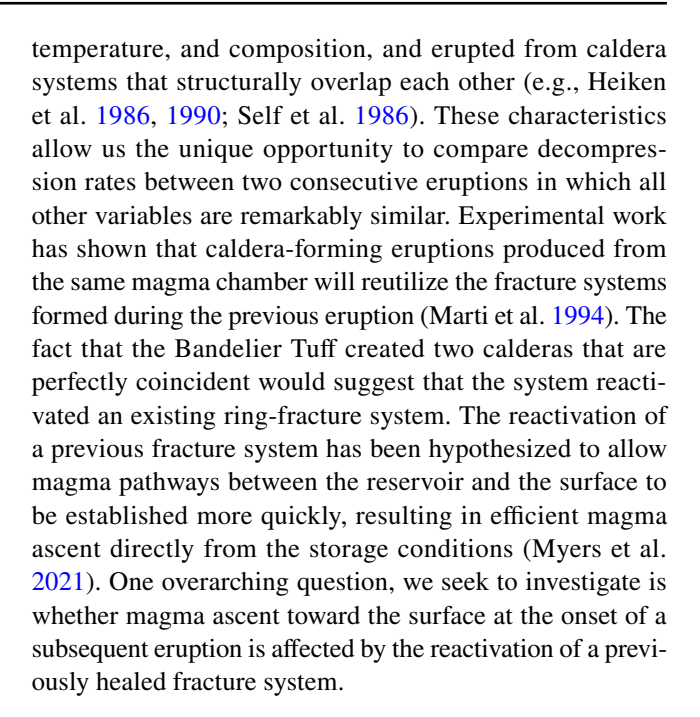
As magma decompresses during its ascent towards the surface, the solubility of volatiles (H₂O, CO₂, S) in the melt decreases, which results in the exsolution of volatiles into a separate fluid phase, and the decrease of their concentration dissolved in the melt. The rate at which magma rises to the surface has a strong control over the behavior of these exsolved volatiles, which in turn directly affects the explosivity of an eruption and modulates explosive/effusive transitions (Eichelberger et al. 1986; Cashman 2004; Castro and Gardner 2008; Cassidy et al. 2018). Constraining variations in magma decompression rates through an eruptive sequence



may help us to better interpret the evolution and timing of these degassing processes and determine how decompression conditions may relate to variations in eruption dynamics. A variety of techniques have been used to estimate decompression rates based on petrologic indicators of volatile loss, including the chemical breakdown of phenocrysts (i.e., amphibole rims; Rutherford and Hill 1993; Rutherford and Devine 2003), microlite nucleation and growth (Hammer et al. 1999; Castro and Gardner 2008), and bubble number density (Toramaru 2006; Hamada et al. 2010). However, in rhyolitic magma, these indicators are limited by kinetics and can only resolve slower decompression histories (days to weeks) or skewed by processes occurring in specific parts of the conduit (i.e., rapid bubble nucleation near the fragmentation front; Mangan et al. 1993; Giachetti et al. 2010; Hajimirza et al. 2021). Thus, many of these methods cannot be applied to study more explosive (often fast) eruptions, involving evolved (kinetically slow) magmas, or for determining decompression rates that represent ascent through the entire conduit system.

One promising technique is to use melt-filled reentrants (unenclosed melt inclusions-herein referred to as reentrants), which have been shown to respond to changing external conditions (degassing) on timescales of minutes to hours (Liu et al. 2007; Humphreys et al. 2008; Lloyd et al. 2014; Ferguson et al. 2016; Myers et al. 2016, 2018, 2021; Newcombe et al. 2020). Modeling of chemical profiles of volatile species in reentrants is a method that can yield an integrated decompression history for rapid rhyolitic magma ascent. For this study, we focus on reentrants in calderaforming systems, where several open questions remain on the dynamics of magma ascent. For instance, reentrants in many of these systems lack measurable CO2, in contrast to the several hundred ppm measured from their co-erupted melt inclusions. Although this has been inferred in some systems to represent an initial slow ascent phase (Myers et al. 2018; Bishop Tuff, USA), there are examples of high H₂O, low CO₂ reentrants that are thought to have quickly ascended from storage (Myers et al. 2021; Santorini, GR). While these studies have shed light on ascent rates of single eruption episodes, no studies have been conducted to compare ascent rates between subsequent eruptive sequences. Lastly, thus far, all reentrant modeling studies of natural systems have only employed a 1D modeling approach, even though the geometry of a reentrant can significantly affect the calculated ascent rate (deGraffenried and Shea 2021). To shed light on some of these open questions, we utilized samples from two subsequent caldera-forming eruptions that together form the Bandelier Tuff, located in northern New Mexico, USA.

The modern-day Bandelier Tuff was erupted as two separate eruptions, which were separated by 350,000 years (Izett & Obradovich 1994; Phillips et al. 2007). A unique aspect of these two eruptions is that they were of similar volume,



Geologic background

The Bandelier Tuff and its associated calderas are a part of the Jemez Mountains Volcanic Field (JMVF) (Fig. 1). The JMVF lies at the intersection of the Jemez Volcanic Lineament and the Rio Grande Rift, where the current spreading rate is < 1 mm/year (Woodward 1977; Savage et al. 1980). The JMVF has been volcanically active for 13 Myr, with the first 11 Myr being dominated mostly by mafic and intermediate volcanism (Aldrich 1986; Wolff and Gardner 1995). The Bandelier Tuff deposit was formed from two calderaforming eruptions, each producing ~ 400 km³ of material. The Otowi member is the first caldera-forming eruption of the JMVF and is dated at 1.61 Ma (Izett & Obradovich 1994). This eruption created the Toledo Caldera, the rim of which is partly exposed northeast of the modern-day Valles Caldera that formed during the second eruption (Fig. 1). The basal unit of the Otowi member is referred to as the Guaje pumice airfall unit, reaching up to 8 m thick. Due primarily to the decrease in coarse pumice fragments, the Guaje pumice developed bedding in the uppermost 2 m of the airfall unit (Crowe et al. 1978; Fig. 2). The upper member of the Bandelier Tuff, formed by the eruption and collapse of the Valles Caldera, is the Tshirege member, dated at 1.26 Ma (Phillips et al. 2007). The Tsankawi pumice, a 3.5-m thick, massive bed of plinian airfall deposits, occurs at the base of the Tshirege member (Fig. 2). In this work, the member names (Otowi/Tshirege) are used when talking about widescale processes occurring within the magma or when referring to the entirety of the deposit including the ignimbrite.



Bulletin of Volcanology (2022) 84:4 Page 3 of 21

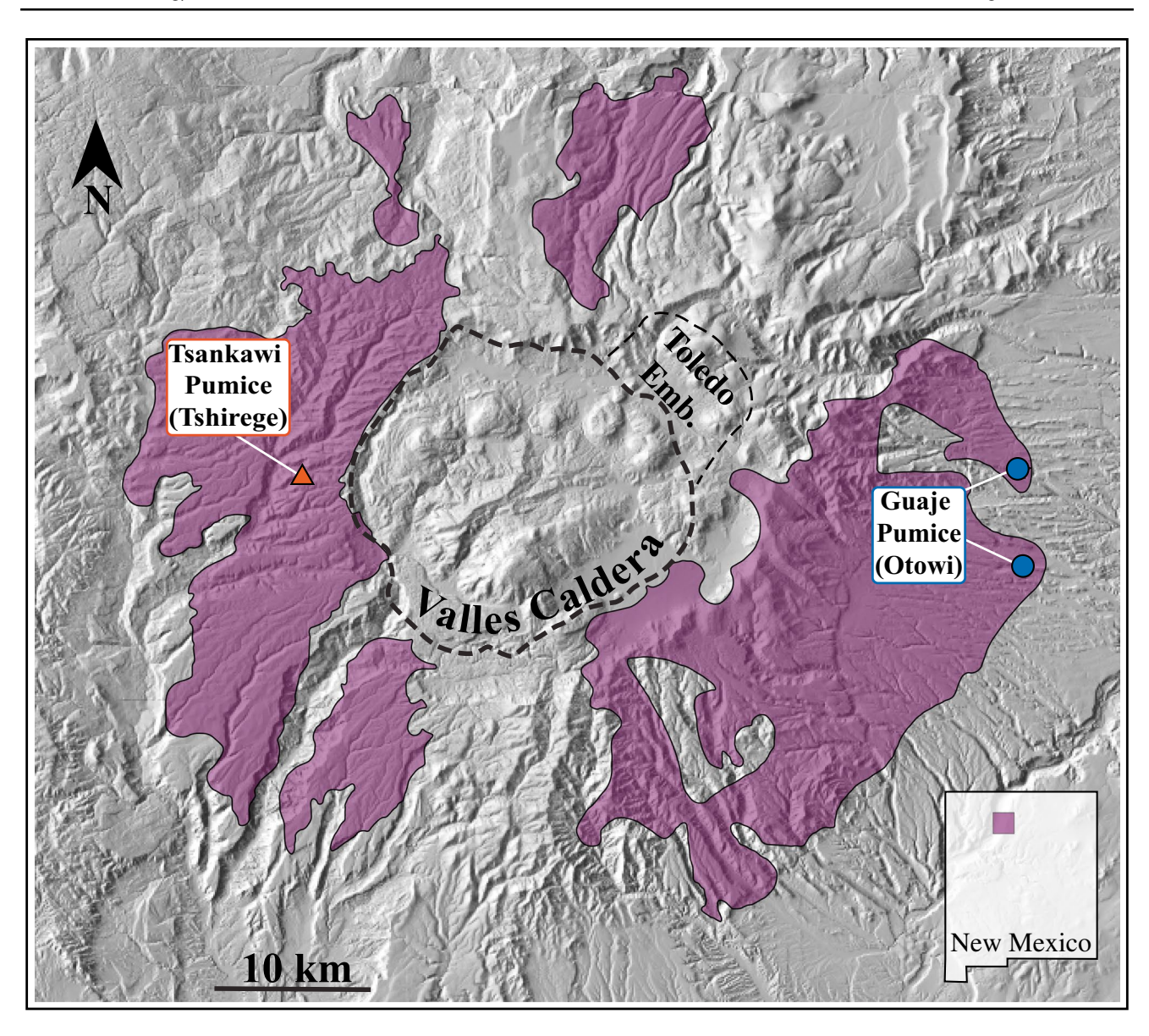


Fig. 1 Map of the modern-day Valles Caldera (thick-dashed line) highlighting the extent of the Bandelier Tuff deposits (purple unit), including Otowi and Tshirege members (modified from Boro et al. 2020). The Valles Caldera is defined by a topographic rim and was formed during the eruption of the Tshirege member (1.26 Ma). It is coincident with the older Toledo Caldera (Otowi member; 1.61 Ma).

The Toledo Embayment (possibly associated with eruptions prior to the Otowi member and currently filled with Cerro Toledo Rhyolite domes) is exposed to the northeast of the Valles Caldera and is outlined by the thin dashed line. Orange and blue symbols highlight sample locations

When specifically referring to the airfall deposit, the unit names (Guaje/Tsankawi) are used.

Stratigraphically constrained geochemical analysis of erupted pumice clasts and bulk ash suggests that a normal compositionally zoned magma chamber fed the eruption of the Tshirege member. This is indicated by a systematic upsection decrease in whole rock SiO₂ content, from ~78 to 70 wt.% (Sussman et al. 2011; Goff et el. 2014). Within this overall normal compositional zonation, the Tshirege member has a distinct region of reverse zoning (more silicic up section) in the late-stage ignimbrite deposits (Goff, et al. 2014).

The Otowi member is less variable in its glass chemistry, with erupted material ranging from ~ 76 to 78 wt.% $\rm SiO_2$ and no relationship between composition and stratigraphic position (Kuentz 1988). However, the Otowi member displays sharp reverse zoning patterns (increase in Sr and Ba concentrations rimward) in quartz and sanidine crystals from the later erupted portions of the ignimbrite, inferred to be records of an increase in magmatic temperature, suggesting that recharge of less evolved material could have triggered the eruption (Wark and Wolff 2006). Similarly, the presence of hornblende dacite pumice fragments in the



4 Page 4 of 21 Bulletin of Volcanology (2022) 84:4

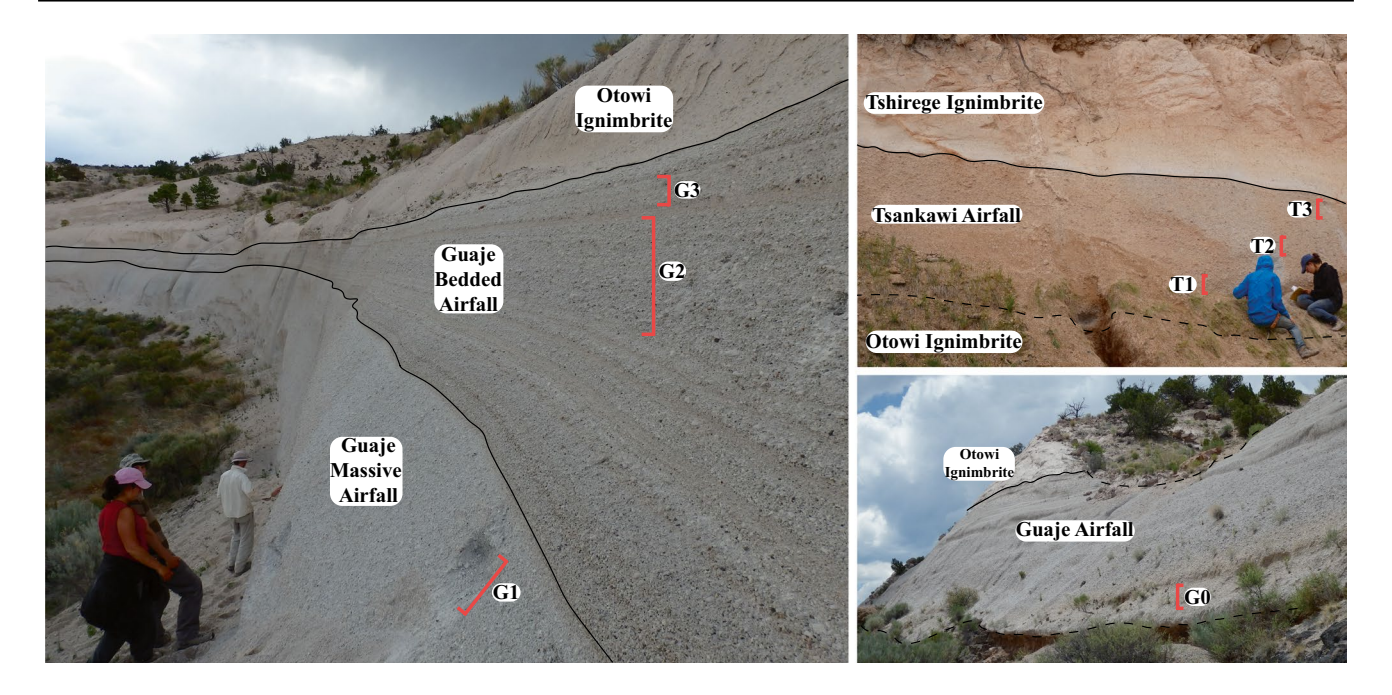


Fig. 2 Field photos showing the stratigraphic boundaries (sub-horizontal black lines) between the Tsankawi (Tshirege Member) and Guaje (Otowi Member) airfall units and their overlying ignimbrites. Locations of whole pumice and bulk samples are bracketed in red

Tshirege member point to the intrusion of an intermediate or mafic magma body as the eruption trigger (Stimac 1996; Boro et al. 2020).

Both eruptions contain 10-20% phenocrysts with an assemblage of alkali feldspar and quartz, with minor amounts of plagioclase, iron-titanium oxides, apatite, zircon, and chevkinite (Smith and Bailey 1966; Goff et al. 2014). The pre-eruption temperature of both airfall deposits was determined to be ~ 700°C based on pyroxene-fayalite thermometry (Warshaw and Smith 1988). This estimate is supported by Ti-in-quartz thermometry (TitaniQ; Wark and Watson 2006) which gives temperatures of ~660–700 °C for the Otowi ignimbrite, and 685-725 °C for the Tshirege ignimbrite (Campbell et al. 2009). Other estimates for the Tsankawi airfall are based on amphibole-liquid (avg. 725 °C) and feldspar-liquid (avg. 736 °C) thermometry (Boro 2019). Additional temperatures for the Otowi ignimbrite are based on zircon saturation thermometry and are higher than estimates from Ti-in-quartz thermometry (819-883 °C; Audétat 2013). The temperature of the Tshirege ignimbrite was also found using Fe-Ti oxides, which yield temperatures of 651-903°°C (avg. 720°°C), and amphibole-melt thermometry, which provides a narrower range ~ 770–810°°C (avg. 797 °C; Boro et al. 2020). From this review, it is clear that the pre-eruptive temperatures for the Bandelier Tuff are widely variable (perhaps stratified) and depend on the thermometer applied.

Quartz-hosted, bubble-free, melt inclusions from the airfall contain variable amounts of H₂O (analyzed by

Fourier-transform infrared—FTIR), ranging from 2.14 to 5.20 wt.%, (avg. 4.05 wt.%) in the Guaje and 1.96 to 5.48 wt.%, (avg. 3.60 wt.%) in the Tsankawi (Waelkens 2021). These values are slightly lower than those measured via ion microprobe by Dunbar and Hervig (1992), where Guaje and Tsankawi melt inclusions range from 3.1 to 6.0 wt.% and 3.5–5.9 wt.% H₂O respectively. Carbon dioxide concentrations in melt inclusions are generally lower in the Tsankawi (<150 ppm), reaching 225 ppm in the top of the Guaje airfall deposit (Waelkens 2021). Based on volatile solubility (Newman and Lowenstern 2002) and the assumption of lithostatic conditions, these combined concentrations correlate to magmatic storage depths of 5-6 km. This is consistent with magma chamber depths of 5-7 km based on fayaliteorthopyroxene barometry and structural modeling (Nielson and Hulen 1984; Warshaw and Smith 1988; Stix and Layne 1996; Goff et al. 2014).

Methods

Sampling and polishing

Seven layers of pumice were sampled from the Tsankawi (3 layers) and Guaje (4 layers) airfall units (Figs. 1, 2). Quartz crystals containing long, tube-like reentrants with large external openings were found in all sampled layers. Qualifying reentrants (glassy, > 100 µm long, bubble at mouth) were picked, mounted to glass slides using crystal



Bulletin of Volcanology (2022) 84:4 Page 5 of 21

bond, and doubly polished along the length of the reentrant. All reentrants had a visible bubble at the mouth that spanned the width of the reentrant, a necessary requirement for diffusive loss of $\rm H_2O$ in an exsolved fluid phase (see Lloyd et al. 2014). We aimed to prepare 3–5 reentrants from each unit, although due to challenges with preparation, some units only yielded 1–2 reentrants. For one of the Guaje layers (sample G0), every crystal shattered during hand-sample preparation, and thus no reentrants were analyzed. Intersected reentrants (9 for the Guaje and 13 for the Tsankawi) ranged from 80 to 250 μm in length, $\sim 20–80~\mu m$ wide at their narrowest point, and most were either tubular or slightly wider toward the interior (Supplementary Fig. 1). Three of the 21 total reentrants measured showed significant narrowing toward the rim.

FTIR H₂O and CO₂ analysis

Freed crystal wafers were analyzed using an FTIR spectrometer at the University of Oregon. Concentrations of $\rm H_2O$ and $\rm CO_2$ were measured with 20–25-µm-square spots along the length of the reentrant. Reentrant lengths allowed for up to 25 FTIR analyses per transect (at 10 µm spacing). Analysis was conducted using a white light source, 256 scans per spot, and a wavelength resolution of 4 (cm $^{-1}$). FTIR absorbances were measured using a linear regression baseline and were converted to concentration by applying the Beer-Lambert law to the relevant baseline-subtracted peak heights (Eq. 1):

$$C = \frac{A \cdot M}{\rho \cdot \epsilon \cdot t} \tag{1}$$

where C is the concentration (wt.%), ρ is the density of rhyolite glass (g/L), M is the molecular mass of the volatile (g/mol), ε is the molar absorbance coefficient (L/mol-cm²), A is the height of the absorbance peak, and t is the thickness of the sample (µm), determined using both a micrometer and the reflectance method of Wysoczanski and Tani (2006). Because ρ and ε are both strongly dependent on water concentration, we assume initial values of 2350 kg/m³ and 80 L·mol⁻¹·cm⁻¹, respectively and then iterate through the calculation until all three values converge (Skirius et al. 1990; Leschik et al. 2004). If the 3550 cm⁻¹ (total water) peak was saturated, water concentrations were measured by using the absorbance peak heights of the 4520 cm⁻¹ bound hydroxyl and 5230 cm⁻¹ molecular water peaks, following the equation of Zhang et al. (1997). Errors for H₂O are calculated using gaussian error propagation and range from ± 0.05 to $0.55 \text{ wt. } \% \text{ (average} = \pm 0.25 \text{ wt.} \%). \text{ For CO}_2, \text{ measured at }$ the 2350 cm⁻¹ (molecular CO₂) peak, all values were found to be below the detection limit of ~20 ppm. Full transect data can be found in Supplementary Table 1.

EPMA major and LA-ICP-MS trace element analysis

Following FTIR analysis, the doubly polished quartz wafers were mounted in 1-inch diameter epoxy mounts for major and trace element analysis at Boise State University. Reentrants were first analyzed on a Cameca SXFive electron microprobe with operating conditions of 15 kV and an unfocused 10-µm beam for all analyses. To evaluate for compositional variability along the length of the reentrant, measurements were taken at 15-μm intervals for reentrants < 150 μm in length. For longer reentrants, measurements were taken every 5 µm for the 30 µm nearest the rim and one additional point was taken at the interior of the reentrant. For each analysis, Si, Na, K, Al, and Fe were measured first using a beam current of 10 nA and then conditions were changed to 50 nA for Mg, Ca, Cl, Ti, and F. Error for each element was calculated using repeat analyses of the standard VG-2 (basaltic glass) and were generally found to be < 1.5% except for FeO (2.5%), Na₂O (4.0%), K₂O (9.7%), F (15.0%), and Cl (24.7%). Trace elements were then analyzed using laser ablation inductively coupled plasma mass spectrometry (LA-ICP-MS) in the Boise State University Isotope Geology Laboratory. Line analyses, 30 µm long by 12 µm wide and perpendicular to the length of the reentrant, were measured at 20 µm spacing and a repetition rate of 10 Hz in order to evaluate trace element variations. For trace element analysis, we used three external glass standards (GSE-1G, ATHO-1G, and T1-G) to evaluate error, with ²⁹Si used as an internal standard. Errors for trace elements were calculated by taking the standard deviation of measured standards from their known values, and were generally found to be less than 12%, except for Zn, Cu, Co, F, and P, which have errors around 22%. Average major and trace element concentrations collected from each transect are listed in Table 1 with the full dataset available in Supplementary Table 2.

Diffusion model setup

Best-fit decompression rates were obtained by simulating measured $\rm H_2O$ profiles using a one-dimensional diffusion MATLAB script (Table 2; Myers et al. 2018). Input parameters required for this model include the starting $\rm H_2O$ and $\rm CO_2$ concentrations (converted to pressure using solubility laws of Liu et al. 2005) and temperature. The model assumes constant decompression, isothermal magma ascent, and equilibrium at the rim/melt boundary. At each time step, a new exterior boundary solubility condition is calculated based on the pressure at that time step. Although the model allows for the input of an exsolved gas content, for all model runs, we assume open-system degassing (gas is removed from the system upon formation). The lack of $\rm CO_2$ in the melt results in a degassing path that is less sensitive to the exsolved gas content; therefore, open-system degassing is



 Table 1 Results of 1D decompression modeling

Reentrant name		Reentrant starting	conditions		Ascent based on reentrant starting conditions								
Tsankawi		Starting pressure (MPa)	Starting CO ₂ (ppm)	Starting H ₂ O (wt. %)	Rim pressure (MPa)	Ascent rate (MPa/s)	dP/dt error (MPa/s)	Ascent time (min)	Ascent rate (m/s), * $F = 1000 \text{ m}$	χ^2			
Тор	T3-1	83.2	20	3.9	10	0.0105	0.0016	116	0.325	0.62			
	T3-3	95.5	20	4.2	30	0.9850		1	41.262	4.81			
Middle	T2-1	71.7	20	3.6	30	0.1000	0.0300	8	3.915	1.00			
	T2-3	83.2	20	3.9	30	0.0162	0.0250	55	0.690	0.19			
	T2-4	37.3	20	2.5	15	0.0014	0.0011	265	0.029	0.14			
	T2-5	100	20	4.3	30	0.0106	0.0030	110	0.443	0.96			
Bottom	T1-1	27.5	20	2.1	10	0.0049	0.0020	60	0.022	0.24			
	T1-2	34.7	20	2.4	20	0.0007	0.0010	350	0.017	0.33			
	T1-3	39.9	20	2.6	10	0.0192	0.0060	26	0.363	0.20			
	T1-4	42.7	20	2.7	15	0.0940	0.0750	5	2.293	0.45			
	T1-5	32.2	20	2.3	20	0.0004	0.0006	508	0.009	0.29			
Guaje													
Bedded airfall	G3-4	132.9	20	5	25	0.0210	0.0100	86	0.821	2.45			
	G3-5	91.4	20	4.1	30	0.0700	0.0300	15	2.950	1.65			
	G3-2	95.6	20	4.2	30	0.1060	0.0700	10	4.447	0.65			
	G2-3	27.5	20	2.1	20	0.0004	0.0015	313	0.004	0.23			
	G2-4	68.1	20	3.5	20	0.0080	0.0030	100	0.278	2.85			
	G2-4	95.6	20	4.2	15	0.0410		33	1.400	0.97			
Massive airfall	G1-2	153	20	5.4	30	0.1000	0.0300	21	4.069	7.06			
	G1-5	95.6	20	4.2	25	0.0170	0.0100	69	0.663	0.40			
Reentrant name		Melt inclusion star	ting conditions		Ascent based on	melt inclusion star							
Tsankawi		Starting pressure (MPa)	Starting CO ₂ (ppm)	Starting H ₂ O (wt. %)	Rim pressure (MPa)	Ascent rate (MPa/s)	dP/dt error (MPa/s)	Ascent time (min)	Ascent rate (m/s), $*F = 1000 \text{ m}$	χ^2			
Top	T3-1	132.9	150	4.64	25	0.0040	0.0015	450	0.153	4.51			
	T3-2	132.9	150	4.64	10	0.0010		2048	0.034	0.15			
	T3-3	132.9	150	4.64	30	0.0650	0.0300	26	2.610	17.86			
Middle	T2-1	120.6	117	4.47	30	0.0050	0.0020	302	0.202	7.29			
	T2-2	120.6	117	4.47	5	0.0010		1927	0.032	0.63			
	T2-3	120.6	117	4.47	30	0.0070	0.0030	215	0.283	4.22			
	T2-4	120.6	117	4.47	15	0.0009	0.0003	1956	0.031	0.18			
	T2-5	120.6	117	4.47	30	0.0080	0.0040	189	0.323	4.75			
Bottom	T1-1	162.1	57	5.48	10	0.0014	0.0005	1811	0.048	0.09			
	T1-2	162.1	57	5.48	20	0.0005	0.0004	4737	0.019	0.30			
	T1-3	162.1	57	5.48	15	0.0049	0.0005	500	0.175	0.33			
	T1-4	162.1	57	5.48	25	0.0048	0.0010	476	0.184	0.64			
	T1-5	162.1	57	5.48	20	0.0003	0.0002	7894	0.011	0.26			

Table 1 (continued)

Guaje										
Bedded airfall	G3-3	162.9	216	5.08	10	0.0012	0.0006	2124	0.042	0.36
	G3-4	162.9	216	5.08	30	0.0120	0.0050	185	0.478	9.62
	G3-5	162.9	216	5.08	30	0.0090	0.0050	246	0.358	17.81
	G3-2	162.9	216	5.08	25	0.0090	0.0050	246	0.358	25.09
	G2-3	162.9	216	5.08	20	0.0003	0.0002	7939	0.011	1.00
	G2-4	162.9	216	5.08	30	0.0030	0.0010	738	0.119	3.85
	G2-4	162.9	216	5.08	30	0.0140	0.0040	158	0.557	4.76
Massive airfall	G1-2	161.8	196	5.11	30	0.0480	0.0300	46	1.911	36.36
	G1-5	161.8	196	5.11	30	0.0070	0.0020	314	0.279	3.63
Reentrant name		High H ₂ O/No CO ₂ starting conditions				melt inclusion starti	ng conditions			
Tsankawi		Starting pressure (MPa)	Starting CO ₂ (ppm)	Starting H ₂ O (wt. %)	Rim pressure (MPa)	Ascent rate (MPa/s)	dP/dt error (MPa/s)	Ascent time (min)	Ascent rate (m/s), *F = 1000 m	χ^2
Тор	T3-1	114.4	0	4.64	10	0.0079	0.0750	220	0.259	0.58
	T3-2	114.4	0	4.64	10	0.0010	0.0010	1740	0.033	0.15
	T3-3	114.4	0	4.64	50	0.0649	_	17	3.444	1.70
Middle	T2-1	106.8	0	4.47	50	0.0028	0.0550	338	0.154	0.53
	T2-3	106.8	0	4.47	35	0.0079	0.1175	151	0.344	0.17
	T2-4	106.8	0	4.47	15	0.0010	0.0100	1530	0.034	0.12
	T2-5	106.8	0	4.47	35	0.0082	0.0525	146	0.357	0.91
Bottom	T1-1	156.4	0	5.48	10	0.0014	0.0350	1743	0.048	0.09
	T1-2	156.4	0	5.48	15	0.0010	0.0025	2357	0.036	0.85
	T1-3	156.4	0	5.48	15	0.0049	0.0825	481	0.175	0.32
	T1-4	156.4	0	5.48	25	0.0048	0.0650	456	0.184	0.64
	T1-5	156.4	0	5.48	20	0.0050	0.0050	4547	0.019	0.47
Guaje										
Bedded airfall	G3-3	135.5	0	5.08	10	0.0012	0.0350	1743	0.041	0.36
	G3-4	135.5	0	5.08	25	0.0210	_	88	0.804	2.39
	G3-5	135.5	0	5.08	30	0.0890	_	20	3.570	1.65
	G3-2	135.5	0	5.08	40	0.0789	0.2425	20	3.496	0.71
	G2-3	135.5	0	5.08	15	0.0006	0.0125	3347	0.021	0.37
	G2-4	135.5	0	5.08	20	0.0048	_	401	0.176	2.62
	G2-4	135.5	0	5.08	30	0.0242	0.2050	73	0.971	0.72
Massive airfall	G1-2	137.0	0	5.11	50	0.1000	_	15	4.931	3.37
	G1-5	137.0	0	5.11	30	0.0097	0.0650	184	0.389	0.37

^{*}Ascent rate calculated using fragmentation depth (F) of 1000 m

a reasonable assumption. Each model run cycled through a range of decompression rates (dP/dt) and fragmentation pressures (P_f) ; where diffusion effectively ceases in the model) to solve for the set of dP/dt and P_f conditions which best approximate the measured data using the diffusivity model of Zhang et al. 2007. Error (also referred to here as misfit) is calculated using the chi-squared goodness of fit test (χ^2) of the calculated volatile gradient compared to the measured gradient (see supplementary material for error calculation). We consider any model with a χ^2 equal to or less than 1 a "good fit" and the model with the lowest χ^2 value is referred to as the "best fit."

Results

Reentrant major and trace element chemistry

Compositions of glass in reentrants from both the Guaje and Tsankawi airfall deposits correspond to high silica rhyolites (76.4–77.6 wt.% SiO2, volatile-free) with indistinguishable major element chemistry, and no noticeable variation between measurements taken from the interior and rim of each reentrant (Fig. 3). Glass data results agree with melt inclusion values taken from Dunbar and Hervig (1992) and glass shard analyses from Westgate et al. (2019) (Fig. 3). The majority of elements (e.g., Na₂O, K₂O, P, Th) lack discernable trends when compared to enriching elements such as SiO₂ or Rb. In contrast, Al₂O₃ and to a lesser extent FeO, show a negative correlation with SiO₂. Between the two eruptions, most trace elements also overlap and span a comparable range of values (e.g., B, P, Nb, Th, Ce). However, some elements are more distinctive between the two eruptions, with volatile (F, Cl) and trace element (Sr, Ba, Zr) concentrations typically higher in the Tsankawi member than the Guaje (Figs. 3, 4). For instance, concentrations of Ba and Sr are found to be at or below detection limit in the Guaje, but significantly higher and clustered in the Tsankawi (Sr: 6–10 ppm and Ba: 16–29 ppm). This separation is likely due to small differences in the extent crystallization of the two magmas, as the concentrations of these elements are largely controlled by the strong partitioning of Ba and Sr into alkali feldspar, the dominant mineral in both eruptions (Fig. 3). Chlorine also distinguishes the two eruptions (although values are within error), with concentrations ranging from 2200–2800 ppm in Guaje and 3200–5600 ppm in Tsankawi, which agree with melt inclusion concentrations (Dunbar & Hervig 1992).

Although no variation in major or trace elements was observed along reentrant transects in either eruption, we do find that transect analyses for nearly all samples show increasing concentrations of Li toward the rim of the reentrant (Fig. 4). Lithium concentrations overlap between

the two eruptions, with interiors from both the Guaje and Tsankawi airfall deposits ranging from 70–100 ppm and rim concentrations preserving higher values of 90–125 ppm. These concentrations are higher than the mean melt inclusion value (~85 ppm) determined from Dunbar and Hervig (1992), although there is significant variability in their melt inclusion data (17–203 ppm Li).

H₂O and CO₂ gradients in REs and 1D modeling

All Bandelier reentrants contain H_2O concentrations ranging from 1.21–5.37 wt.% in the interior, with normal gradients going to lower concentrations at the rims (0.65–4.14 wt.%). Although interior H_2O concentrations represent a large variation, values mimic the range measured from co-erupted melt inclusions (2.0–5.2 wt.%; Fig. 5; Waelkens 2021). Reentrant H_2O contents are generally higher in the Guaje samples (n=9), with average interior concentrations of 3.63 wt.% compared to 2.80 wt.% in the Tsankawi samples (n=13). All measured reentrant profiles lack detectable CO_2 (detection limit ~ 20 ppm) (Fig. 5; Waelkens 2021).

As volatile diffusivity is strongly temperature dependent, we applied the Boehnke et al. (2013) zircon saturation thermometer to our samples. This thermometer returned temperatures of 823 ± 23 °C (2 σ) for the Guaje airfall and 835 ± 81 °C for the Tsankawi airfall. Although these temperatures align very well with the results from Audétat (2013) using the same method on ignimbrite samples (819–883 °C), they are significantly higher than the ~700–800 °C estimate for both airfall deposits provided by other thermometers (e.g., Warshaw and Smith 1988; Campbell et al. 2009; Boro et al. 2021). As temperature is crucial for diffusion modeling, we consider the implications of a large temperature uncertainty in determining decompression rates but choose to represent the results based on the lowest temperature to provide conservative decompression estimates.

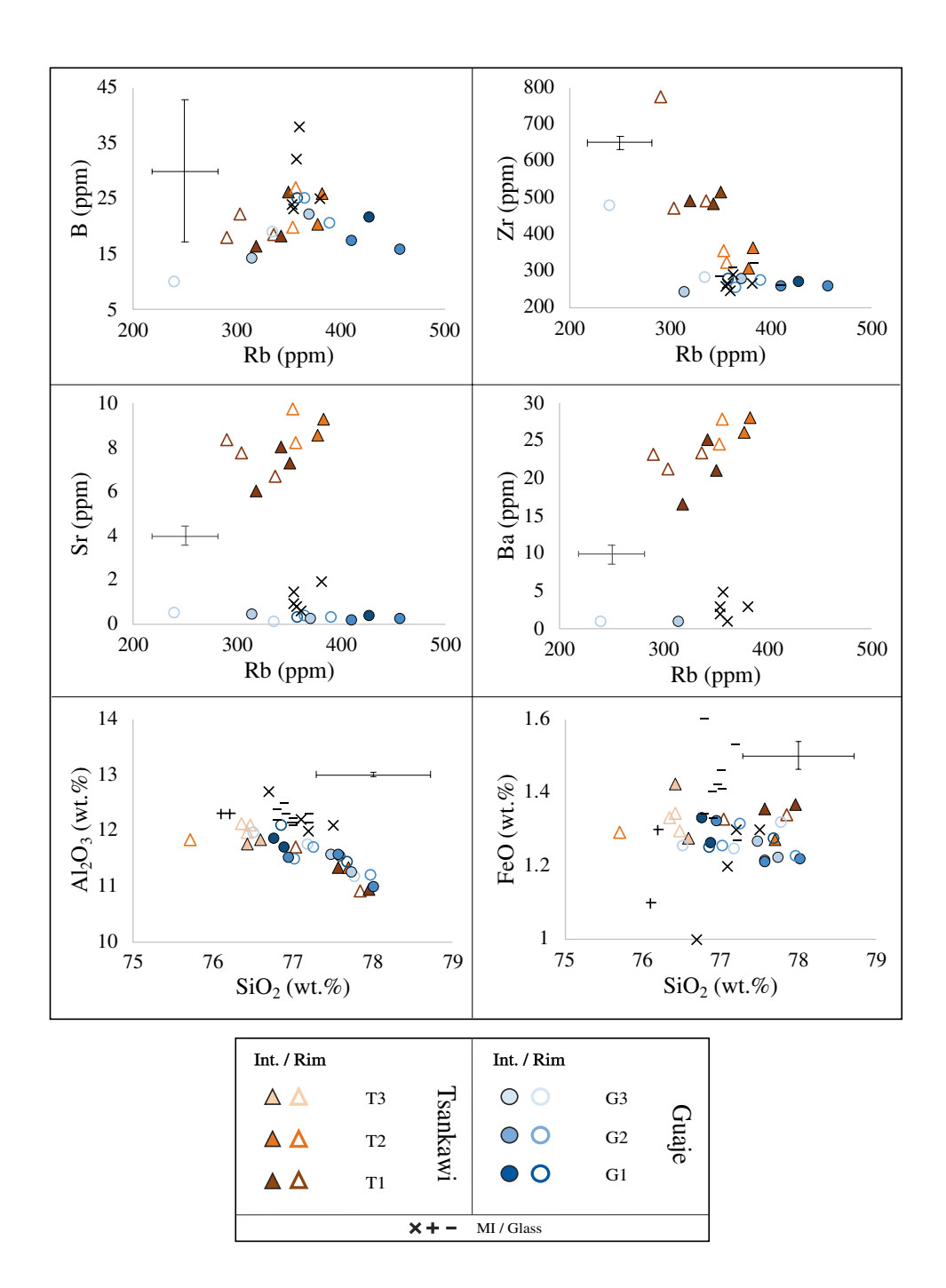
Starting H₂O and CO₂ concentrations for model runs have traditionally been chosen based on measured melt inclusion data (high H₂O/high CO₂ ascent from storage), or by using the volatile concentrations found in the innermost part of the reentrant (moderate H₂O/no CO₂; reset by an initial stalling or slow ascent phase; e.g., Myers et al. 2018; Fig. 6); we explore both options here and present a third alternative (high H₂O/no CO₂). We note that many caldera-forming, silicic systems exhibit a reduction or absence of measurable CO₂ concentrations in reentrants in comparison to melt inclusions from the same deposits (Liu et al. 2007; Myers et al. 2018; 2021). However, most reentrants still contain relatively high H₂O concentrations. Although this has now been noted in multiple systems, including the Bandelier, the implications of this observation are still unclear. We envision two potential explanations: (1) late-stage, isobaric crystallization drove CO₂



Table 2 Summary of good profile fits (χ^2 misfits < 1) from the decompression model, based on starting conditions from reentrant (RE) and melt inclusion (MI). Based on these results, we determined the average ascent rate for all model conditions

	All conditions	No CO ₂	RE	MI	No fit	No CO ₂ start (m/s)	RE start (m/s)	MI start (m/s)
Tsankawi $(n=13)$	6	11	10	8	1	0.149	1.15	0.03
Guaje $(n=9)$	1	5	4	2	4	0.984	1.70	0.04

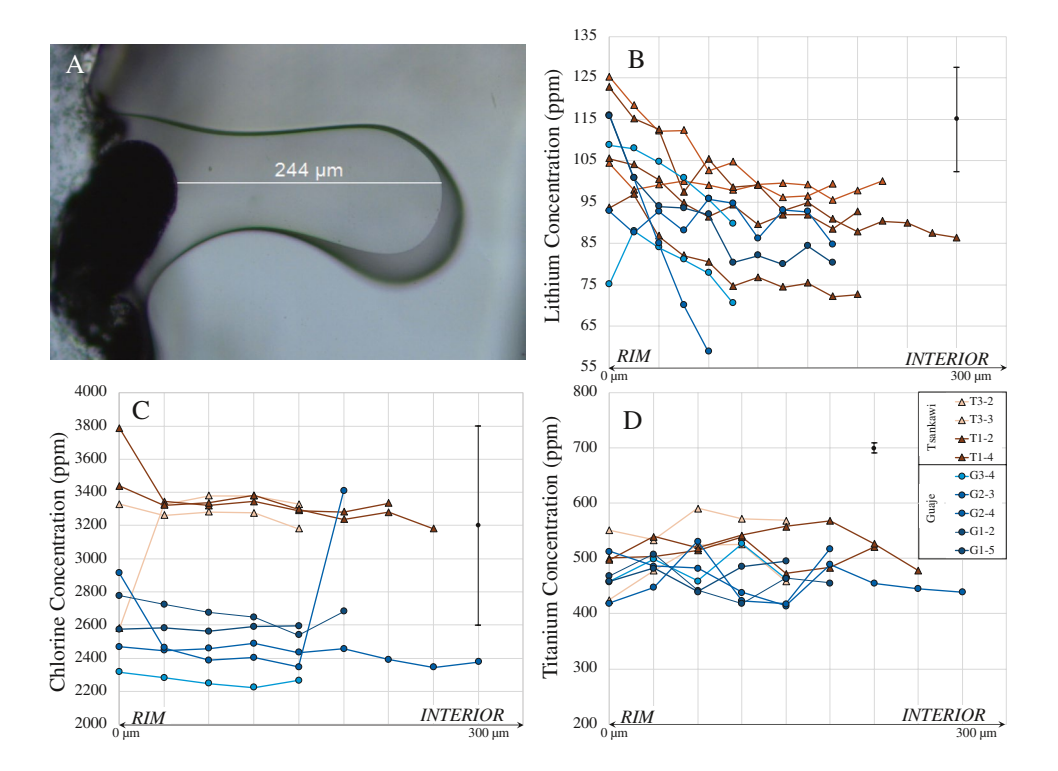
Fig. 3 Compositional plots of select major and trace element concentrations. Circles and triangles represent reentrant analysis, either near the opening of the reentrant (open symbol) or in the interior (closed symbol). Errors represent 1σ standard deviation on repeat standard glass analyses. Melt inclusion data from plinian airfall deposits by Dunbar and Hervig (1992) is shown as plus signs (Tsankawi) and crosses (Guaje). Tsankawi glass shard data from Westgate et al. (2019) is indicated by dashes. Blue symbols represent reentrants from the Guaje fall unit and burnt orange symbols represent samples from the Tsankawi fall unit





4 Page 10 of 21 Bulletin of Volcanology (2022) 84:4

Fig. 4 A Photomicrograph of reentrant 03A-3 (Guaje). B, C, D Transect trace element analyses of Li, Cl, and Ti where each symbol represents a single-point analysis, with profiles going from reentrant rims (left) toward reentrant interiors (right). Blue symbols represent reentrants from the Guaje fall unit and burnt orange symbols represent samples from the Tsankawi fall

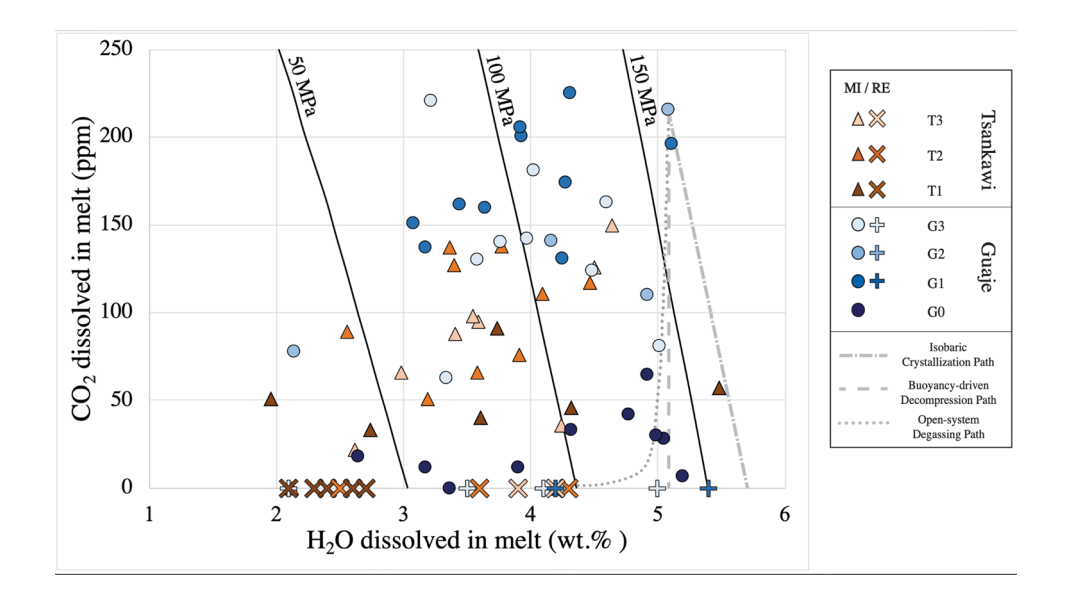


into a fluid phase, removing all traces from the reentrant through diffusive re-equilibration or (2) a small decompression event occurred, driving the remaining CO_2 , into the fluid phase, followed by re-equilibration of the reentrant to a H_2O saturated pressure. This re-equilibration to low CO_2 conditions would require 10 s of hours to days to occur (based on solubility and diffusivity of CO_2 ; Liu et al. 2005; Zhang et al. 2007). Although we later discuss the probability of each scenario for the Bandelier system, for now, we accept that both ideas result in a *high* H_2O , *no* CO_2 starting melt for modeling reentrant profiles. The

third series of diffusion models therefore explored the scenario where only the melt inclusion-derived H_2O was present in the reentrants initially and CO_2 had already degassed (referred to hereafter as the "high H_2O /no CO_2 " starting condition). This third scenario eliminates the need for a slow initial ascent/stalling event required by the reentrant interior starting condition.

We find that most diffusion profiles from the Guaje can *only be* fit using the *moderate* H_2O/no CO_2 reentrant interior measurements (n = 4 of 9) or the *high* H_2O/no CO_2 as starting conditions (n = 5 of 9), with only two

Fig. 5 Water and CO₂ concentrations of melt inclusions (MI; Waelkens (2021)) and innermost reentrant data (RE), where each symbol represents a single MI or RE. Isobars (solid lines) and open-system degassing (dotted grey line) pathway calculated using Volatile Calc (Newman & Lowenstern 2002). Dashed gray lines highlight two separate scenarios for exsolving CO2 from the melt (isobaric crystallization and buoyancydriven decompression), producing the high H₂O, low CO₂ starting pressures. This was found to produce better model fits to measured RE profiles





Bulletin of Volcanology (2022) 84:4 Page 11 of 21

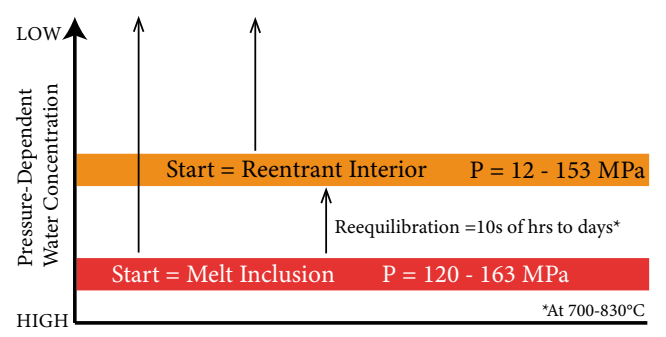
successfully fit using the high H₂O/high CO₂ melt inclusions as starting conditions (Table 3). Four of nine could not be fit with any of these starting conditions. For the Tsankawi samples, the majority of profiles (n = 11)of 13) are fit using either the reentrant interior or high H₂O/no CO₂ start, with 8 of 13 able to be fit using the melt inclusion start; one profile could not be fit with any starting condition (Table 3). There is no correlation between calculated ascent rate and stratigraphic position for either eruption (Supplementary Fig. 2). However, we do find that the model generally fits the data better in the Tsankawi than in the Guaje reentrants, in which the measured interior water concentrations are rarely fit, with model results providing significantly lower H₂O concentrations (Supplementary Fig. 2). The better model fits found for the Tsankawi reentrants could suggest that the assumptions laid out in our model (constant ascent from some starting condition) better recreates the natural dataset in the Tsankawi member, where magma ascent occurs more directly from storage to the surface without stalling and reequilibrating in the conduit. By contrast, some aspect of the Guaje ascent is being missed by our current framework Fig. 7.

Based on reentrant starting conditions (moderate $H_2O/no\ CO_2$), successful best-fit decompression rates for the Guaje range from 0.0012–0.1060 MPa/s, overlapping with the Tsankawi 0.0003–0.1000 MPa/s. Decompression rates using melt inclusion–starting conditions are slower (~1 to 1.5 orders of magnitude) than those recovered using the reentrant start, whereas the best-fit decompression rates for the high $H_2O/no\ CO_2$ models fall in between. The results of decompression modeling using each of the three starting conditions are shown in Fig. 8. In most cases, the Guaje samples record decompression rates that are similar to the Tsankawi, however, are generally associated with poorer model fits when applying the

melt inclusion-derived starting conditions ($high\ H_2O/high\ CO_2$). Presented decompression rates were determined using a temperature of 700 °C; however, we evaluate the error of this assumption by presenting rates for the fastest and slowest reentrants at the higher temperature estimate of 830 °C. This increased temperature increases the decompression rates by 340–440% (Fig. 8).

2-Dimensional diffusion modeling

A major assumption of the reentrant models presented here is that diffusion occurs only along 1 dimension, parallel to the length of the reentrant, from the interior to the mouth. However, natural reentrants have complicated 3D geometries that impact diffusive flux pathways and thus the assumption of 1D diffusion may introduce significant error on determined decompression rates (deGraffenried and Shea 2021). A common reentrant geometry that challenges the 1D assumption is when the reentrant constricts towards the mouth (e.g., Fig. 4a). This constriction creates a "bottlenecking effect," where diffusion is slowed and results in higher water concentrations being recorded further into the reentrant than would be expected when compared to a perfect cylindrical geometry (deGraffenried and Shea 2021). To evaluate the effects of complex natural reentrant geometries on our modeled decompression rates, we implemented a 2D model based on deGraffenried and Shea (2021). The 2D model was modified to use the same water diffusivity as the 1D code (Zhang et al. 2007). All 2D modeling was conducted using the conservative Bandelier temperature of 700 °C, the same initial and fragmentation pressures as the 1D model, and the reentrant interior starting conditions. Due to computational limitations, and the fact that the chosen parameters resulted in very good model fits, we chose not to iterate through different fragmentation pressures or starting conditions. We selected only four reentrants to evaluate,



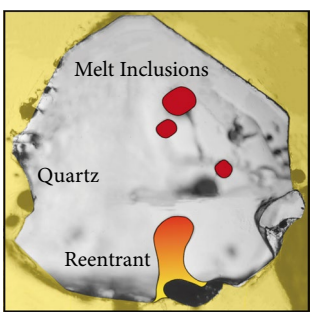


Fig. 6 Schematic diagram illustrating the melt inclusion vs. the reentrant starting conditions. Using the melt inclusion concentrations to derive starting pressures indicates magma ascent directly from storage conditions without any major stalling (left long arrow). Starting pressures derived from the reentrant interior volatile concentrations

require an initial slow ascent and re-equilibration to lower saturation pressures (middle short arrow) prior to the final ascent (right arrow). Re-equilibration times are calculated based on solubility and diffusivity of H₂O and CO₂ (Liu et al. 2005; Zhang et al. 2007)



Table 3 Average major and trace element concentrations, including 1σ error (average deviation of all analyses), for the five reentrants from the Tsankawi member, and eight reentrants from the Otowi member

	Tsankay	wi major e	lements			,	Error (1σ)
(wt.%)	T1-2	T1-4	T2-2	T3-1	T3-2	T3-3	(wt.%)
SiO_2	77.59	77.62	76.70	76.41	77.46	76.54	0.71
TiO ₂	0.05	0.05	0.05	0.06	0.05	0.06	0.00
Al_2O_3	11.45	11.10	11.59	12.11	11.25	11.90	0.04
FeO	1.35	1.36	1.28	1.31	1.36	1.30	0.03
MgO	0.02	0.03	0.03	0.03	0.01	0.03	0.00
CaO	0.25	0.26	0.25	0.28	0.24	0.28	0.00
Na ₂ O	4.56	4.38	4.90	4.61	3.98	4.52	0.18
K ₂ O	4.11	4.59	4.37	4.53	5.04	4.71	0.44
Cl	0.34	0.33	0.56	0.32	0.32	0.33	0.09
F	0.29	0.28	0.29	0.34	0.29	0.34	0.05
		wi trace el					Error (1σ)
(ppm)	T1-2	T1-4	T2-2	T3-1	T3-2	T3-3	(ppm)
Li	77.5	95.0	131.7	130.4	71.7	131.3	14.5
Be	17.8	23.6	18.7	5.8	9.7	11.7	6.2
В	19.7	21.8	24.2	21.8	29.5	24.2	10.0
P	59.3	46.3	51.0	43.3	40.9	38.8	11.2
Sc	3.3	4.0	0.3	0.1	b.d.l	1.2	0.3
V	0.5	1.0	b.d.l	0.2	b.d.l	0.2	0.1
Cr	15.0	17.9	0.7	b.d.l	b.d.l	7.7	5.3
Mn	714.8	705.5	696.7	577.9	681.4	583.1	72.6
Co	0.4	0.8	0.2	0.2	0.2	0.1	0.1
Ni	0.9	0.8	1.4	2.8	2.7	2.7	0.3
Cu	6.7	1.2	1.6	b.d.l	1.9	b.d.l	0.7
Zn	143.3	145.1	144.4	174.3	226.7	172.8	36.8
Ga	26.9	27.1	30.6	30.3	31.8	30.8	3.1
Rb	323.9	326.6	376.2	349.0	428.8	357.8	45.9
Sr	6.3	7.6	5.4	9.1	0.6	7.8	0.7
Y	176.5	167.2	123.1	61.9	63.5	65.7	12.8
Zr	507.2	476.4	355.8	196.7	217.9	210.4	37.9
Nb	237.9	236.8	212.3	181.7	210.9	183.1	26.5
Cs	11.7	11.8	13.4	12.3	15.3	12.9	1.6
Ba	19.1	22.4	20.0	28.8	2.0	28.0	2.6
La	60.4	59.3	40.9	29.9	28.2	30.7	4.8
Ce	107.3	108.9	94.6	94.1	92.5	95.6	11.3
Pr	12.4	12.0	9.3	7.3	6.6	7.2	1.0
Nd	47.0	44.3	33.7	24.1	22.0	25.4	4.2
Sm	13.4	13.1	9.3	6.1	6.0	6.0	1.0
Eu	0.0	0.0	0.0	0.0	b.d.l	0.0	0.0
Gd	17.1	16.4	10.5	7.2	6.8	6.9	1.3
Tb	3.4	3.3	2.3	1.4	1.3	1.3	0.2
Dy	25.8	24.3	17.6	9.7	10.0	10.5	1.7
Но	5.6	5.3	4.1	2.1	2.1	2.1	0.4
Er	17.2	15.7	11.3	6.4	6.3	6.4	1.1
Tm	2.8	2.5	2.0	0.9	1.0	1.1	0.2
Yb	17.3	16.1	11.8	6.3	6.6	6.7	1.1
Lu	2.8	2.7	1.9	1.1	1.0	0.9	0.2
Hf	25.2	22.3	16.6	8.9	10.2	9.8	1.8
Ta	17.2	15.7	13.6	10.3	10.3	10.2	1.4
Pb	56.8	55.8	66.0	63.2	76.3	64.2	6.1
Th	51.4	48.2	34.8	22.7	23.1	22.8	3.7



 Table 3 (continued)

U	14.3	14.1	15.9	15.9	18.5	15.9	1.9		
	Guaje n	najor elem	ents						Error (1σ)
(wt.%)	G2-3	G2-4	G2-4	G3-4	G3-5	G3-2	G1-2	G1-5	(wt.%)
SiO_2	77.46	77.66	77.53	77.67	77.26	77.19	76.78	77.03	0.71
${ m TiO_2}$	0.05	0.05	0.05	0.05	0.05	0.05	0.05	0.05	0.00
Al_2O_3	11.33	11.48	11.54	11.24	11.66	11.78	12.00	11.70	0.04
FeO	1.25	1.22	1.28	1.27	1.25	1.23	1.28	1.27	0.03
MgO	0.02	0.01	0.02	0.01	0.02	0.02	0.01	0.01	0.00
CaO	0.26	0.24	0.26	0.26	0.26	0.26	0.26	0.25	0.00
Na_2O	4.16	4.47	4.31	4.08	4.31	4.27	4.65	4.40	0.17
K_2O	4.98	4.44	4.54	4.96	4.72	4.75	4.43	4.80	0.46
Cl	0.24	0.23	0.27	0.23	0.22	0.28	0.27	0.26	0.06
F	0.27	0.21	0.22	0.23	0.25	0.18	0.27	0.24	0.04
	Guaje tı	race eleme	ents						Error (1σ)
(ppm)	G2-3	G2-4	G2-4	G3-4	G3-5	G3-2	G1-2	G1-5	(ppm)
Li	90.9	122.7	86.2	67.2	103.3	79.5	96.1	90.3	12.6
Be	26.4	14.4	b.d.l	16.4	13.3	b.d.l	14.7	33.6	8.4
В	21.9	18.3	20.7	20.9	19.0	12.6	22.3	21.8	8.4
P	83.9	44.6	82.2	50.9	33.2	65.8	47.9	78.9	14.7
Sc	3.5	b.d.l	2.8	b.d.l	b.d.l	10.9	b.d.l	1.6	0.7
V	b.d.l	0.1	b.d.l	b.d.l	0.1	0.5	b.d.l	0.3	0.0
Cr	13.2	7.5	7.1	b.d.l	2.0	27.2	5.4	13.9	5.6
Mn	687.1	636.8	710.8	608.2	603.3	610.5	695.8	683.6	72.0
Co	0.7	b.d.l	0.3	b.d.l	b.d.l	b.d.l	0.3	0.6	0.1
Ni	1.8	1.6	2.1	1.5	1.8	2.0	1.6	1.7	0.2
Cu	b.d.l	0.3	b.d.l	0.3	b.d.l	b.d.l	18.9	0.1	1.1
Zn	139.0	128.2	135.1	146.0	135.8	98.7	129.3	136.7	28.7
Ga	29.4	28.3	29.9	26.2	27.3	24.5	27.6	29.2	2.9
Rb	412.0	424.2	420.1	383.1	392.3	285.6	401.1	392.1	49.5
Sr	0.3	0.1	0.4	0.1	0.1	0.4	0.2	0.3	0.0
Y	93.6	102.6	93.3	79.9	78.9	99.1	107.4	95.6	10.9
Zr	265.6	286.2	261.8	219.6	221.0	282.1	307.3	279.7	30.7
Nb	258.1	250.0	259.3	209.5	207.0	188.1	248.5	265.0	29.7
Cs	13.2	14.2	14.1	10.9	11.7	8.8	13.0	13.4	1.5
Ba	b.d.l	0.0	b.d.l	0.2	0.3	0.8	1.5	b.d.l	0.1
La	32.4	30.8	30.1	30.6	29.8	41.4	33.6	30.2	3.7
Ce	91.7	83.6	86.7	88.9	88.0	99.2	84.3	85.5	10.1
Pr	8.8	8.3	8.4	8.7	8.6	10.6	8.8	8.3	1.0
Nd	33.8	32.3	31.8	32.1	29.9	40.9	33.5	30.3	4.2
Sm	9.4	9.9	9.0	9.5	9.3	11.3	10.8	9.1	1.1
Eu	0.0	0.0	0.0	0.0	0.0	b.d.l	0.0	0.0	0.0
Gd	10.7	10.3	10.3	10.1	9.7	12.4	11.6	10.5	1.3
Tb	2.1	2.3	2.0	2.0	2.0	2.4	2.4	2.0	0.2
Dy	15.0	15.6	13.9	13.7	13.4	16.8	17.5	14.5	1.5
Но	3.1	3.4	2.9	2.8	2.9	3.5	3.6	3.1	0.3
Er	9.2	9.9	8.8	8.2	7.9	9.1	10.8	9.1	1.0
Tm	1.5	1.6	1.5	1.3	1.2	1.5	1.8	1.4	0.1
Yb	9.3	10.1	9.2	8.2	7.9	9.5	11.1	9.3	1.0
Lu	1.4	1.6	1.4	1.2	1.2	1.6	1.7	1.5	0.1
Hf	12.4	13.5	11.4	11.1	9.7	12.9	14.5	13.0	1.4
Та	17.4	17.1	17.7	13.8	13.4	13.3	17.7	17.7	1.7
Pb	53.3	50.8	55.0	47.2	46.9	38.7	53.0	54.8	4.8



4	Page 14 of 21	1							olcanology	(2022) 84	(2022) 84:4	
Table 3	(continued)	 Th	40.7	41.6	39.5	31.7	32.0	37.8	44.3	40.1	4.2	

22.6

again because of the computational intensity associated with a 2D model, representing the full range of observed reentrant shapes: necked 0% (tubular), 24%, 38%, and 44% (strongly necked). The degree of necking was calculated by dividing the narrowest part of the reentrant by the widest. In theory, the tubular reentrant should record nearly identical ascent rates using the 1D and 2D methods, and as the degree of necking increases, the difference between the two methods should also increase.

U

22.2

20.3

As predicted, we found that the non-necked reentrant retrieved a best-fit 2D decompression rate that was identical to 1D (Fig. 9). The 24% necked reentrant returned a slightly slower decompression rate (0.0185 MPa/s in 2D vs. 0.0192 MPa/s in 1D), whereas the most strongly necked reentrant (44% necked) fit a decompression rate 27% slower than the 1D results (0.0036 MPa/s vs. 0.0049 MPa/s). Lastly, the 38% necked reentrant was the only sample that produced a decompression rate that was *faster* when using the 2D model, by 50% (0.0328 MPa/s vs. 0.0162 MPa/s). This may be due to the diffusion front interacting with a more complex 3D morphology. While the 2D model returns slightly different best-fit values than the 1D model, it is important to note that all 2D model results are within the misfit uncertainty of the 1D model. Full results are shown in Fig. 9,

Supplementary Fig. 3, and can be found in Supplementary Table 3.

21.0

22.4

2.4

Discussion

18.3

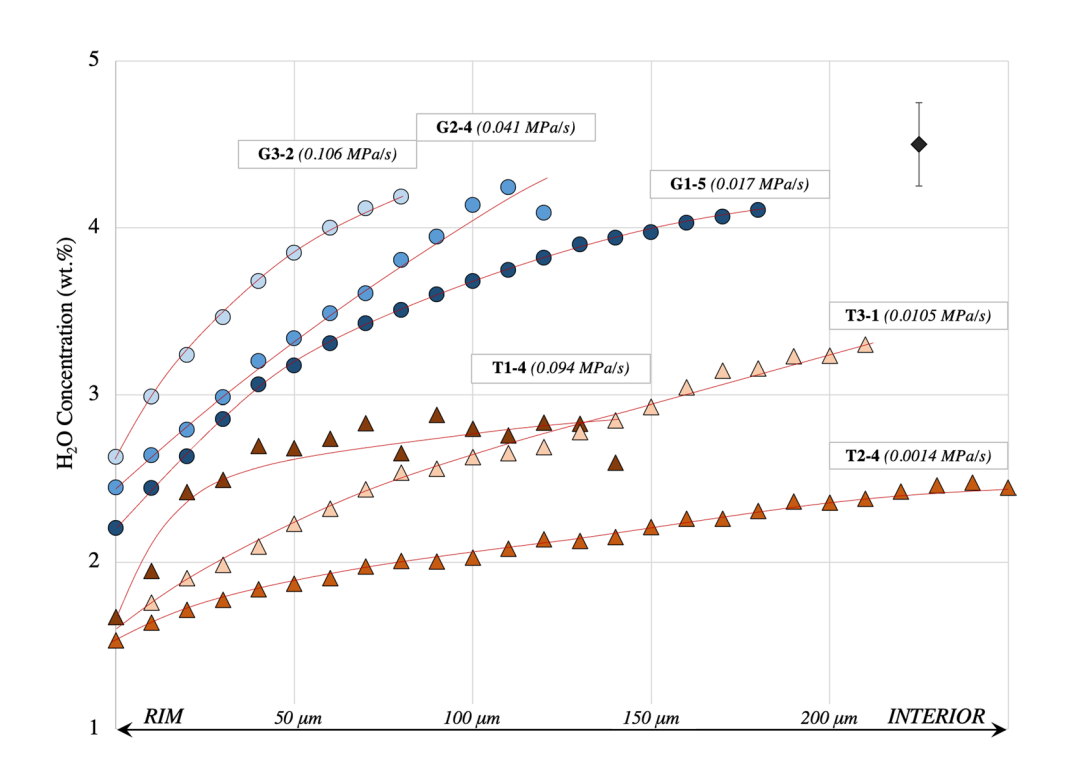
19.2

14.5

Lithium gradients

Although most major and trace elements show little to no significant difference between units or within a given reentrant, lithium concentrations near the mouths of each reentrant increase by up to 55 ppm above interior compositions, an increase of $\sim 25\%$. Charlier et al. (2012) also found reverse gradients in Li preserved in feldspar and quartz phenocrysts for the Oruanui supereruption (NZ). To explain this observation, they postulate that during the very last stages of decompression (less than ~ 22 MPa, 125 to 720 s before quenching) interactions between LiCl and high-temperature steam caused a hydrolysis reaction, affecting the partitioning of Li and resulting in a 50% increase of Li concentration in crystal rims. Thus, there is potential that a similar mechanism was occurring in the Bandelier tuffs, with the breakdown of a fluid phase in the shallow conduit system. This reaction should also result

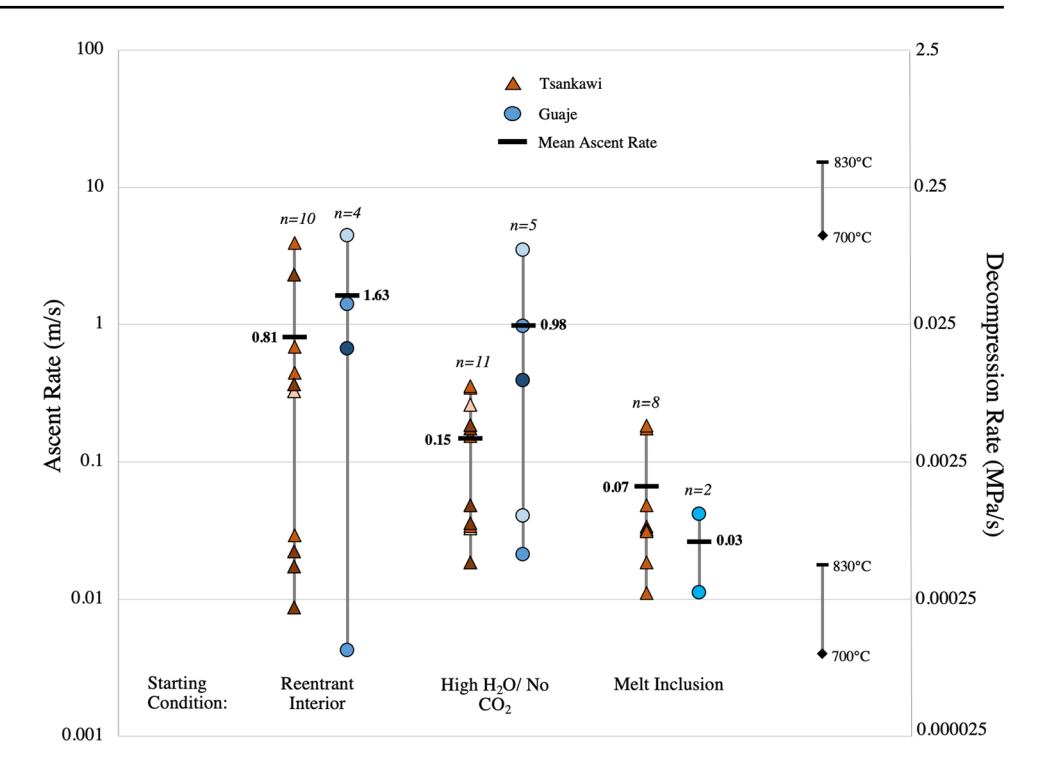
Fig. 7 Examples of water transect data collected by FTIR, with each symbol representing a single point analysis, and each line representing the best-fit decompression rate for one reentrant from an individual layer. Error bar represents average analytical error of ± 0.25 wt.% H₂O. Blue symbols represent reentrants from the Guaje fall unit and burnt orange symbols represent samples from the Tsankawi fall unit. The labels contain the best-fit decompression rate obtained via 1-D diffusion modeling using the reentrant interior starting conditions. Full transect data is available in Supplementary Table 1





Bulletin of Volcanology (2022) 84:4 Page 15 of 21 4

Fig. 8 Results of decompression modeling using three different starting conditions, where bestfit decompression rates (MPa/s) were translated into ascent rate (m/s) (see "Comparison with other caldera-forming systems' for discussion). Each symbol represents a single reentrant. Best fits for the largest number of reentrants were achieved using the reentrant interior and high H₂O/no CO₂ starting conditions. The error bar presented represents the shift in the determined ascent rate based on a 130 °C temperature increase (see "H2O and CO2 gradients in REs and 1D modeling" for discussion). This approach as applied to both the slowest and fastest ascent rate, which results in a 340-440% shift



in large amounts of Cl partitioning into the fluid phase; however, gradients of Cl in all Bandelier reentrants are lacking. Although a diffusion coefficient for Li in hydrous rhyolite melt has been determined (Holycross et al. 2018), this does not take into account how Li would react during degassing and ascent. Thus, modeling Li profiles would require too many assumptions about its behavior to provide meaningful results. While the cause of lithium gradients preserved in reentrant glasses of the Bandelier are currently unknown and beyond the scope of this paper, the application of Li diffusion as eruption chronometer remains an exciting avenue for future work.

Decompression rates for the Tsankawi and Guaje eruptions

When $\rm H_2O$ diffusion in more than one direction is taken into account, we find that the best-fit decompression rate of reentrants with a necked geometry differ from their 1D best-fit decompression rates by up to 50% (Fig. 9). While the reentrant geometry clearly affects the decompression rate, the best-fit rates in 2D and in 1D are still within the uncertainty range of each other for all geometries tested. This indicates that the reentrant geometry is not a significant factor affecting rates extracted from Bandelier reentrants and conclude that diffusion modeling in 1D is sufficient for reasonable geometries (necking < 50%). In contrast, the error introduced by modeling at a higher temperature results in a more dramatic change (~300–500% difference). But importantly, both of these error sources pale in comparison to the

three orders of magnitude variation represented by each airfall deposit (Fig. 8). This highlights the extreme variations in ascent dynamics experienced over the course of a single eruption, and that accurate quantification of ascent rate cannot be accomplished through limited petrological sample sizes.

Evaluating the 1D results, decompression rates recorded by reentrants from the Guaje and Tsankawi initial airfall deposits are largely indistinguishable for all starting conditions (Fig. 9). However, a major difference is that the majority of Tsankawi samples can be modeled using all three starting conditions, whereas the Guaje samples can only be fit using the moderate H₂O/no CO₂ reentrant interior or the high H₂O/no CO₂ starting conditions. Additionally, a higher number of Guaje reentrants (n=4) cannot be fit by any modeling scenario. We interpret these observations to suggest that the Guaje likely experienced an initial period of slower ascent (hours to days) deeper in the conduit and reequilibrated at a lower pressure before its final ascent (e.g., Figs. 2, 4). Although this idea explains part of our dataset, half of the Guaje reentrants cannot be fit from any starting condition. Our only interpretation to explain this result if that there is an assumption built into our model (e.g., constant-rate decompression) that is not recreating the ascent history of this system. In contrast, Tsankawi reentrants are likely recording a decompression event with little or no stalling in the conduit. This suggests that the Tsankawi magma, the second of the two caldera-forming eruptions, was able to develop a conduit system more effectively, potentially exploiting some preexisting weakness (e.g., interpretation of



4 Page 16 of 21 Bulletin of Volcanology (2022) 84:4

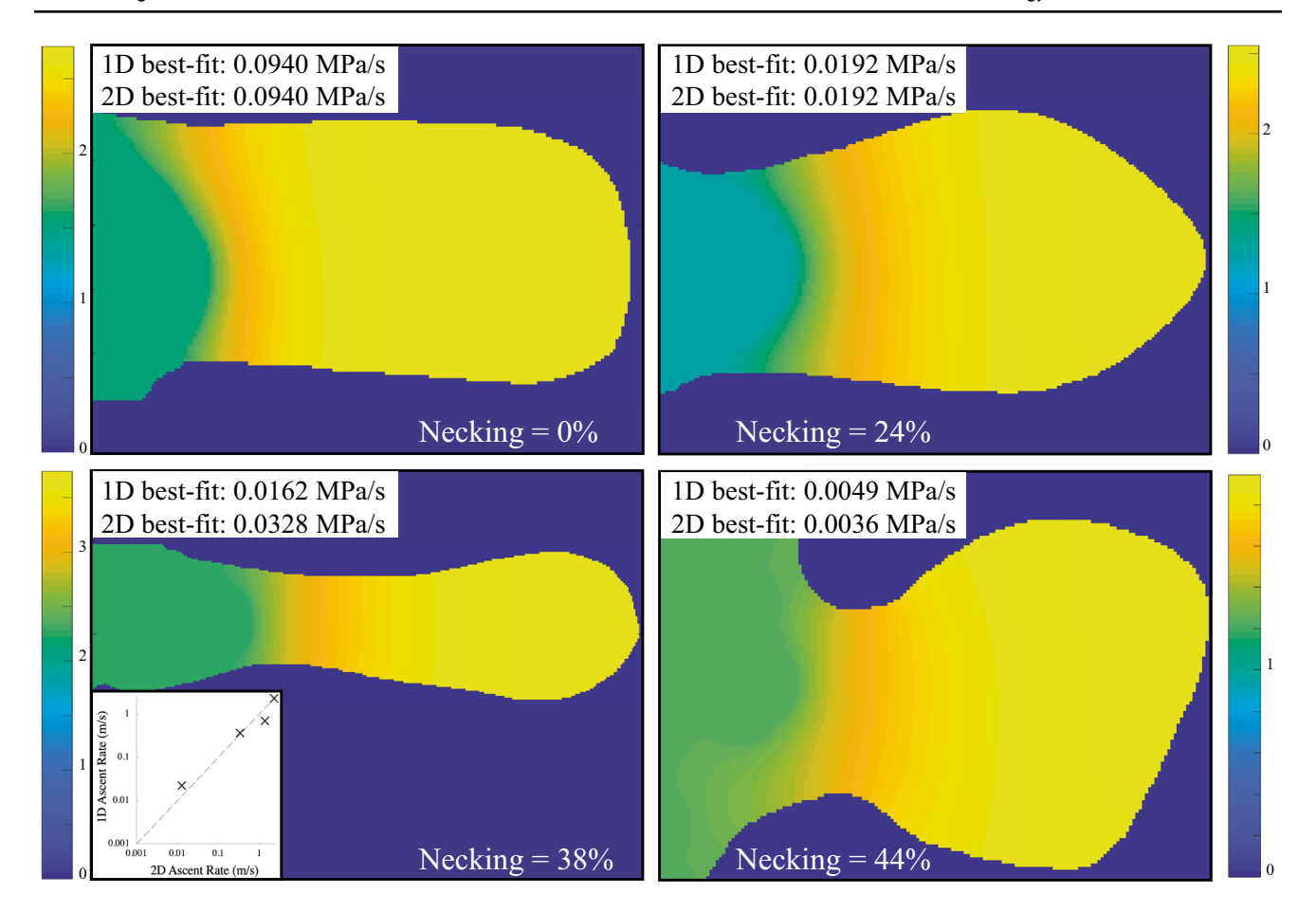


Fig. 9 Results of diffusion modeling in two dimensions (2D) for four Tsankawi reentrants with different necking ratios. Color gradients and correlated scale bar represent water concentration in weight percent.

Necking ratio is determined by dividing the width of the narrowest part of the reentrant by the widest part. Inset chart shows comparison of ascent rates in 1D vs. 2D, dashed gray line is 1:1 line

Myers et al. 2021). Regardless of the initial opening behavior, the remarkable overlap in the integrated decompression rate of these two systems, especially compared to the range observed in rhyolitic systems (see "Comparison with other caldera-forming systems"), suggests that regional stress, crustal structure, and intrinsic magma properties may ultimately control ascent rates of rhyolite magma.

Comparison with other caldera-forming systems

Although both the reentrant interior and the high $\rm H_2O/$ no $\rm CO_2$ models provide good fits to a similar number of reentrants in the two fall deposits, here we present ascent rates based on the reentrant interior volatile concentration in order to draw comparisons with other caldera-forming systems. Decompression rates can be converted to ascent rates through converting the starting pressure into depth using the assumption of lithostatic conditions, assuming a fragmentation depth of 1000 m (Myers et al. 2018), and applying an assumed crustal density of 2600 kg/m³. Ascent rates obtained for the Guaje reentrants range from

0.28–4.45 m/s, and again, largely overlap with the Tsankawi (0.32–3.92 m/s). These ascent rates obtained for the Bandelier members are comparable to those of other rhyolitic caldera-forming eruptions, most notably the results from the Oruanui (0.06–3.47 m/s) and Huckleberry Ridge (0.25–3.88 m/s) eruptions, which both show large scatter of H₂O compositions in enclosed melt inclusions, similar to that of the Bandelier melt inclusions (Myers et al. 2018; Fig. 10). However, these rates are much slower than those determined for the Bishop Tuff (0.4–12.99 m/s; Fig. 10) and the Bronze-Age eruption of Santorini (0.4–11 m/s; Myers et al. 2021). Notably, the opening behavior of both the Oruanui and Huckleberry Ridge eruptions is thought to be modulated by tectonic forces (Myers et al. 2016, 2018).

Removal of CO₂: implications for silicic caldera-forming eruptions

It has been observed that reentrants measured from several silicic, caldera-forming eruptions (e.g., Oruanui, Bishop Tuff, Santorini), commonly contain little or no CO₂, while



Bulletin of Volcanology (2022) 84:4 Page 17 of 21

coexisting melt inclusions have concentrations up to several hundred ppm (Myers et al. 2018, 2021). Similarly, the Guaje and Tsankawi reentrants lack detectable CO₂ compositions compared to their melt inclusion counterparts. In fact, most reentrants here require CO₂ to be absent from their starting conditions in order to retrieve good model fits (Fig. 8). This observation suggests that reentrants in most silicic systems are recording the removal of CO₂ from the melt into a fluid phase prior to final ascent where water begins to exsolve and degas. One way to remove CO₂ from the system is represented by the moderate H₂O/no CO₂ reentrant interior starting condition, where an initial stage of decompression occurs prior to stalling and re-equilibration. This initial stage of ascent would require a significant decompression event (upwards of 100 MPa) to remove CO₂ and lower H₂O, however, is unsatisfactory in that it requires different starting pressures for each reentrant (starting pressures range from 12 to 153 MPa). An alternative model for which we found successfully modeled the majority of reentrants is one that maintains the high H₂O content, but removes the CO₂ fully from the system. As previously mentioned in "H₂O and CO₂ gradients in REs and 1D modeling," we have proposed two mechanisms: late-stage crystallization and a minor decompression event (less than ~ 30 MPa), which we model below to explore their validity. One final explanation for the lack of CO₂ observed in reentrants compared to their corresponding melt inclusions is that of a multi-stage ascent model; however, that is beyond the scope of this paper.

The first idea we explore is that additional isobaric crystallization occurred for both the Otowi and Tshirege magmas after melt inclusion entrapment, driving H₂O enrichment, and CO₂ exsolution into a fluid phase. To determine if this process could occur due to a feasible amount of crystallization (e.g., less than the crystallinity of the erupted magma), we modeled crystallization along a cooling path using rhyolite-MELTs (Gualda et al. 2012; Ghiorso and Gualda 2015). Conditions used for MELTs modeling are provided in the Supplementary Material. Starting with H₂O/CO₂ conditions based on melt inclusion concentrations from the highest pressure (~ 160 MPa) for each layer, we allowed temperature to drop, trigger crystallization and driving H₂O enrichment, until all CO2 was removed from the system. The results of this modeling suggest that this process would only require 7–13% of additional crystallization, well within the range of the erupted products (5-20%: Kuentz 1988).

The second method explored was a small buoyancy-driven decompression event, in which magma density decreases due to small amounts of fractional crystallization or volatile exsolution, causing the magma to rise buoyantly within the storage region. The amount of decompression

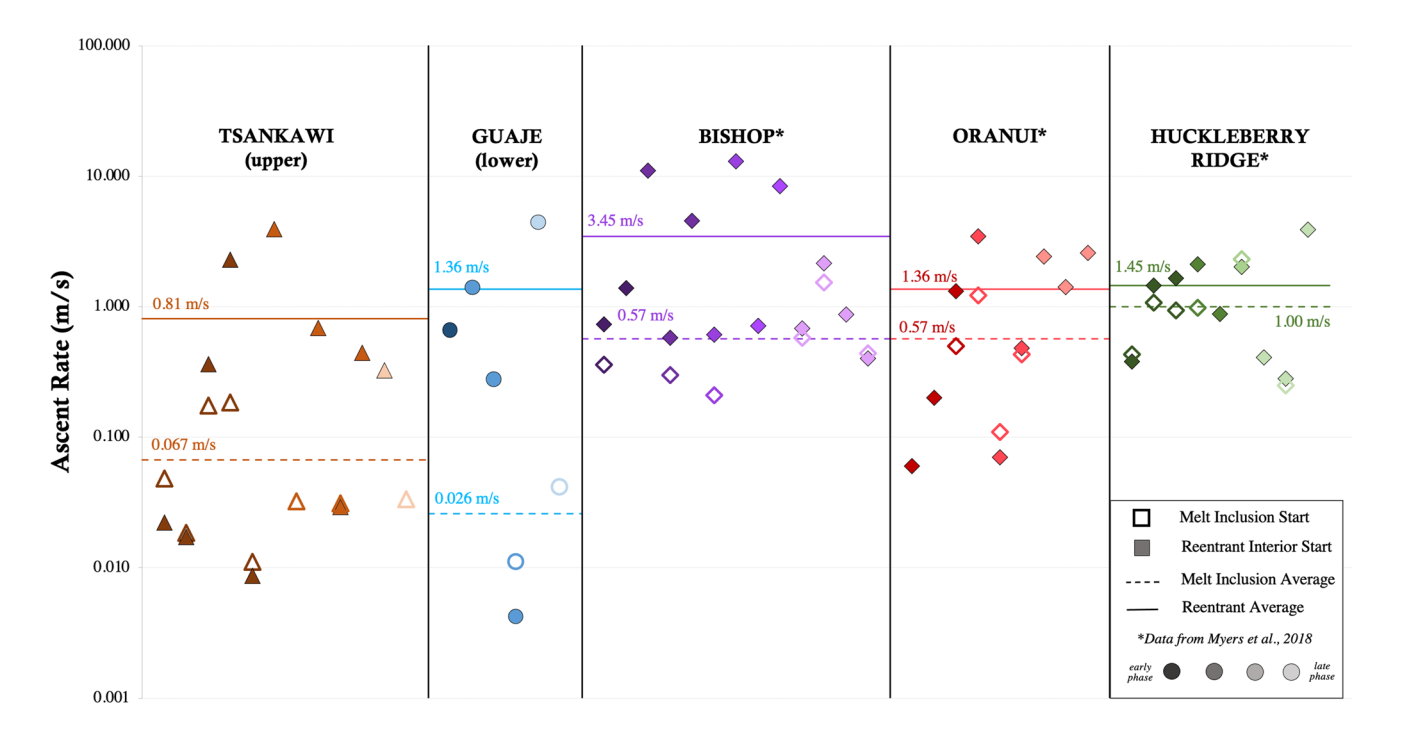


Fig. 10 Comparison of ascent rates obtained from 1D reentrant volatile diffusion from the Tsankawi and Guaje airfalls to studies of other caldera-forming eruptions (Myers et al. 2018). Model starting conditions are determined by the saturation pressure from either the volatile content of the interior of the reentrant (solid shapes) or the volatile content of melt inclusions (open shapes). Labeled horizontal bars

indicate the average ascent rate for each eruption based on reentrant (solid line) and melt inclusion (dashed line) starting conditions, with melt inclusion starts generally resulting in slower ascent rates. Darker colors represent samples from earlier eruption phases and lighten towards later eruption phases



4 Page 18 of 21 Bulletin of Volcanology (2022) 84:4

required to drive CO₂ from the system was determined assuming open-system degassing, and based on solubility/ pressure relationships taken from VolatileCalc (Newman and Lowenstern 2002; Fig. 5). Starting H₂O/CO₂ conditions were based on the melt inclusion with the highest CO₂ for each layer. For both the Otowi and Tshirege magmas, a small drop in pressure (7-28 MPa, equivalent to 0.3-1.1 km) is required to evolve from melt inclusion-starting conditions to a CO₂-free system, while still maintaining a high-water concentration. The necessary decrease in pressure is highest in the upper layers of each member, requiring 28 MPa in the Guaje and 20 MPa in the Tsankawi. The lowest layer of the Guaje requires the smallest pressure decrease (7.1 MPa), while the middle and lower layers of the Tsankawi require intermediate pressure decreases (16 and 12 MPa, respectively).

This process of consistent CO₂ removal in late-stage silicic chambers could be significant, because it would support the existence of a pre-eruptive exsolved fluid phase. Although overpressurization of the magma chamber (i.e., via injection of new magma) is often called upon as the triggering mechanism for smaller volcanic eruptions, including for both Bandelier units, large-scale magma chambers (> 1000 km³) may require a different triggering mechanism to initiate movement toward the surface (Jellinek and DePaolo 2003; Gregg et al. 2012). One mechanism that has been suggested is buoyancy-driven overpressurization, by which a volatilerich buoyant magma layer forms near the top of the chamber and creates enough overpressure to initiate diking and potentially lead to eruption (McLeod and Tait 1999; Caricchi et al. 2014; Malfait et al. 2014). Our results suggest that only a small drop in pressure is necessary to remove CO₂ from the system. This small pressure change could be a record of early diking and decompression events in the upper portion of the magmatic system prior to eruption onset (Papale et al. 2017).

Another classic internal triggering mechanism is due to isobaric crystallization in a closed system, where additional crystallization promotes the exsolution of a volatile phase, leading to internal instability and eruption of the magma chamber (Fowler and Spera 2008; Tramontano et al. 2017). Tramontano et al. (2017) demonstrate that only ~ 10% crystallization under fluid saturated conditions is required to reach the suggested ~ 25 MPa overpressure threshold to trigger eruption. The amount of crystallization necessary to remove $\rm CO_2$ from the Bandelier reentrants (determined via MELTS modeling to be 7–13%) thus would more than likely create enough overpressure to drive the start of eruption, assuming a saturated system.

These two scenarios are both plausible for removing CO_2 from the Guaje and Tsankawi magmas, and likely exert feedback on each other, making it difficult to identify a dominant process. The observed lack of CO_2 in reentrants may

therefore be recording the internal triggering mechanisms responsible for initiating eruption of the Tsankawi magma. However, several of the Guaje samples are still unable to be modeled using the high H₂O/No CO₂ starting condition; thus, if the Guaje samples are recording these processes of CO₂ removal, they are then being overprinted by a more complex ascent path.

Conclusions

This study sought to examine the effect of a previous caldera-forming eruption on the ascent rate of subsequent eruptions and to thoroughly evaluate the assumptions in the reentrant volatile diffusion modeling technique used to extract magma ascent dynamics, through application to the Guaje and Tsankawi airfall units of the Bandelier Tuff. Notably, this work is the first to compare ascent rates of two eruptions from an overlapping caldera complex, as well as the first to compare 1D and 2D diffusion models in natural samples. The major results are as follows:

- 1) Ascent rates obtained for the Guaje and Tsankawi members do not show significant differences; however, we found that many of the later erupted Tsankawi reentrants could be successfully modeled using the melt inclusion starting conditions, whereas the Guaje reentrants yielded better fits using shallower, reentrant starting conditions. This indicates a slow initial decompression of the Guaje magma, while the Tsankawi magma was able to rise more directly from depth. We interpret this to suggest that the latter eruption was able to establish a connected conduit system earlier on in the eruption, but that this process does not correlate to a change in ascent rate. Rather, the remarkable similarity between ascent rates from these two eruptions could point to the importance of regional stress, crustal structure, and intrinsic magma properties to modulating magma ascent.
- 2) Comparisons of diffusion models in 1D and 2D reveal that reentrant geometry effects decompression rates by as much as 50%. However, the 1D and 2D results are within the model uncertainty of each other. We find that temperature uncertainty has a large effect on modeled decompression rates, resulting in a 340–440% increase in ascent rate when applying the large temperature uncertainty ranging from 700 to 830 °C. This is the largest source of uncertainty within the model and highlights the importance of constraining the pre-eruptive temperature.
- 3) Each airfall deposit shows three orders of magnitude of variation in ascent rate, suggesting that a few reentrants from one layer are not enough to constrain the variation of magma ascent within a given eruption.



Bulletin of Volcanology (2022) 84:4 Page 19 of 21

4) The absence of CO₂ in reentrants compared to their coexisting melt inclusions is a common occurrence in silicic eruptions. The removal of CO₂ indicates a preeruptive exsolution event and is potentially a record of eruption triggering. We investigate two CO₂ removal mechanisms—isobaric crystallization and initial decompression, potentially due to buoyancy—and find that both mechanisms are reasonable for removing CO₂ from these systems, and possibly supporting eruption onset.

Supplementary Information The online version contains supplementary material available at https://doi.org/10.1007/s00445-021-01518-4.

Acknowledgements This work is supported by EAR award 1922513 to M. Myers. Computational efforts were performed on the Hyalite High Performance Computing System, operated and supported by University Information Technology Research Cyberinfrastructure at Montana State University. The authors thank T. Fischer, R.J. Bodnar, and one anonymous reviewer for their thorough and constructive feedback which has greatly improved this manuscript.

Author contribution Megan Saalfeld and Madison Myers contributed to the study conception and design. Material preparation, data collection and analysis were performed by Megan Saalfeld. Development of the 2D code was done by Rebecca deGraffenried and Thomas Shea. Sample collection and melt inclusion analysis was performed by Clara Waelkens. The first draft of the manuscript was written by Megan Saalfeld and all authors commented on previous versions of the manuscript. All authors read and approved the final manuscript.

Funding This work is supported by EAR award 1922513 to M. Myers.

Data availability All collected data is available as tables in the supplementary material.

Declarations

Conflict of interest The authors declare no competing interests.

References

- Aldrich M Jr (1986) Tectonics of the Jemez lineament in the Jemez Mountains and Rio Grande rift. J Geophys Res Solid Earth 91:1753–1762
- Audétat A (2013) Origin of Ti-rich rims in quartz phenocrysts from the Upper Bandelier Tuff and the Tunnel Spring Tuff, southwestern USA. Chem Geol 360:99–104
- Boehnke P, Watson EB, Trail D, Harrison TM, Schmitt AK (2013) Zircon saturation re-revisited. Chem Geol 351:324–334
- Boro JR (2019) Recharge and mobilization of crystal mush to produce and erupt a zoned magma chamber–the Tshirege Member of the Bandelier Tuff. Valles Caldera, New Mexico
- Boro JR, Wolff JA, Neill OK (2020) Anatomy of a recharge magma: Hornblende Dacite Pumice from the rhyolitic Tshirege Member of the Bandelier Tuff. Valles Caldera, New Mexico, USA: Contributions to Mineralogy and Petrology 175:1–26
- Boro JR, Wolff JA, Neill OK, Steiner AR, Ramos FC (2021) Titanium diffusion profiles and melt inclusion chemistry and morphology in

- quartz from the Tshirege Member of the Bandelier Tuff: American Mineralogist. J Earth Planet Mater 106:620–632
- Campbell ME, Hanson JB, Minarik WG, Stix J (2009) Thermal history of the Bandelier magmatic system: evidence for magmatic injection and recharge at 1.61 Ma as revealed by cathodoluminescence and titanium geothermometry. J Geol 117:469–485
- Caricchi L, Annen C, Blundy J, Simpson G, Pinel V (2014) Frequency and magnitude of volcanic eruptions controlled by magma injection and buoyancy. Nat Geoscie 7:126–130
- Cashman KV (2004) Volatile controls on magma ascent and eruption. v. 150. American Geophysical Union Geophysical Monograph Series, Washington DC, p. 109-124
- Cassidy M, Manga M, Cashman K, Bachmann O (2018) Controls on explosive-effusive volcanic eruption styles. Nat Commun 9:1-16
- Castro JM, Gardner JE (2008) Did magma ascent rate control the explosive-effusive transition at the Inyo volcanic chain, California? Geology 36:279–282
- Charlier B, Morgan D, Wilson C, Wooden J, Allan A, Baker J (2012) Lithium concentration gradients in feldspar and quartz record the final minutes of magma ascent in an explosive supereruption. Earth Planet Sci Lett 319:218–227
- Crowe BM, Linn GW, Heiken G, Bevier ML (1978) Stratigraphy of the Bandelier tuff in the Pajarito plateau: applications to waste management. Los Alamos National Laboratory Informal Report LA-7225-MS
- deGraffenried R, Shea T (2021) Using volatile element concentration profiles in crystal-hosted melt embayments to estimate magma decompression rate assumptions and inherited errors. Geochem Geophys Geosyst 22:e2021GC009672
- Dunbar NW, Hervig RL (1992) Volatile and trace element composition of melt inclusions from the Lower Bandelier Tuff: implications for magma chamber processes and eruptive style. J Geophys Res Solid Earth 97:15151–15170
- Eichelberger J, Carrigan C, Westrich H, Price R (1986) Non-explosive silicic volcanism. Nature 323:598–602
- Ferguson DJ, Gonnermann HM, Ruprecht P, Plank T, Hauri EH, Houghton BF, Swanson DA (2016) Magma decompression rates during explosive eruptions of Kīlauea volcano. Hawaii, Recorded by Melt Embayments: Bulletin of Volcanology 78:71
- Fowler SJ, Spera FJ (2008) Phase equilibria trigger for explosive volcanic eruptions. Geophys Res Lett 35:L08309
- Ghiorso MS, Gualda GA (2015) An H 2 O-CO 2 mixed fluid saturation model compatible with rhyolite-MELTS. Contrib Mineral Petrol 169:1–30
- Giachetti T, Druitt TH, Burgisser A, Arbaret L, Galven C (2010) Bubble nucleation, growth and coalescence during the 1997 Vulcanian explosions of Soufrière Hills Volcano, Montserrat. J Volcanol Geotherm Res 193:215–231
- Goff F, Warren R, Goff CJ, Dunbar N (2014) Eruption of reversezoned upper Tshirege Member, Bandelier Tuff from centralized vents within Valles caldera, New Mexico. J Volcanol Geoth Res 276:82–104
- Gregg P, De Silva S, Grosfils E, Parmigiani J (2012) Catastrophic caldera-forming eruptions: Thermomechanics and implications for eruption triggering and maximum caldera dimensions on Earth. J Volcanol Geotherm Res 241:1–12
- Gualda GA, Ghiorso MS, Lemons RV, Carley TL (2012) Rhyolite-MELTS: a modified calibration of MELTS optimized for silicarich, fluid-bearing magmatic systems. J Petrol 53:875–890
- Hajimirza S, Gonnermann HM, Gardner JE (2021) Reconciling bubble nucleation in explosive eruptions with geospeedometers. Nat Commun 12:1–8
- Hamada M, Laporte D, Cluzel N, Koga KT, Kawamoto T (2010) Simulating bubble number density of rhyolitic pumices from Plinian



4 Page 20 of 21 Bulletin of Volcanology (2022) 84:4

- eruptions: constraints from fast decompression experiments. Bull Volcanol 72:735–746
- Hammer JE, Cashman KV, Hoblitt R, Newman S (1999) Degassing and microlite crystallization during pre-climactic events of the 1991 eruption of Mt Pinatubo, Philippines. Bull Volcanol 60:355–380
- Heiken G, Goff F, Gardner JN, Baldridge W, Hulen J, Nielson DL, Vaniman D (1990) The Valles/Toledo Caldera Complex, Jemez Volcanic Field, New Mexico. Annu Rev Earth Planet Sci 18:27–53
- Heiken G, Goff F, Stix J, Tamanyu S, Shafiqullah M, Garcia S, Hagan R (1986) Intracaldera volcanic activity, Toledo caldera and embayment, Jemez Mountains, New Mexico. J Geophys Res Solid Earth 91:1799–1815
- Holycross M, Watson E, Richter F, Villeneuve J (2018) Diffusive fractionation of Li isotopes in wet, highly silicic melts. Geochem Perspect Lett 6:39–42
- Humphreys MC, Menand T, Blundy JD, Klimm K (2008) Magma ascent rates in explosive eruptions: constraints from H2O diffusion in melt inclusions. Earth Planet Sci Lett 270:25–40
- Izett GA, Obradovich JD (1994) 40Ar/39Ar age constraints for the Jaramillo Normal Subchron and the Matuyama-Brunhes geomagnetic boundary. J Geophys Res Solid Earth 99:2925–2934
- Jellinek AM, DePaolo DJ (2003) A model for the origin of large silicic magma chambers: precursors of caldera-forming eruptions. Bull Volcanol 65:363–381
- Kuentz DC (1988) The Otowi member of the Bandelier Tuff: A study of the petrology, petrography, and geochemistry of an explosive silicic eruption, Jemez Mountains, New Mexico. Master's Thesis, University of Texas at Arlington
- Leschik M, Heide G, Frischat G, Behrens H, Wiedenbeck M, Wagner N, Heide K, Geißler H, Reinholz U (2004) Determination of H2O and D2O contents in rhyolitic glasses. Phys Chem Glas 45:238–251
- Liu Y, Zhang Y, Behrens H (2005) Solubility of H2O in rhyolitic melts at low pressures and a new empirical model for mixed H2O-CO2 solubility in rhyolitic melts. J Volcanol Geother Res 143:219-235
- Liu Y, Anderson AT, Wilson CJ (2007) Melt pockets in phenocrysts and decompression rates of silicic magmas before fragmentation. J Geophys Res Solid Earth 112:B06204
- Lloyd AS, Ruprecht P, Hauri EH, Rose W, Gonnermann HM, Plank T (2014) NanoSIMS results from olivine-hosted melt embayments: magma ascent rate during explosive basaltic eruptions. J Volcanol Geother Res 283:1–18
- Malfait WJ, Seifert R, Petitgirard S, Perrillat J, Mezouar M, Ota T, Nakamura E, Lerch P, Sanchez-Valle C (2014) Supervolcano eruptions driven by melt buoyancy in large silicic magma chambers. Nat Geosci 7:122–125
- Mangan MT, Cashman KV, Newman S (1993) Vesiculation of basaltic magma during eruption. Geology 21:157–160
- Marti J, Ablay G, Redshaw LT, Sparks R (1994) Experimental studies of collapse calderas. J Geol Soc 151:919–929
- McLeod P, Tait S (1999) The growth of dykes from magma chambers. J Volcanol Geotherm Res 92:231–245
- Myers ML, Wallace PJ, Wilson CJ, Morter BK, Swallow EJ (2016) Prolonged ascent and episodic venting of discrete magma batches at the onset of the Huckleberry Ridge supereruption, Yellowstone. Earth Planet Sci Lett 451:285–297
- Myers ML, Wallace PJ, Wilson CJ, Watkins JM, Liu Y (2018) Ascent rates of rhyolitic magma at the onset of three caldera-forming eruptions. Am Mineral 103:952–965
- Myers ML, Druitt TH, Schiavi F, Gurioli L, Flaherty T (2021) Evolution of magma decompression and discharge during a Plinian event (Late Bronze-Age eruption, Santorini) from multiple eruption-intensity proxies. Bull Volcanol 83:1–17

- Newcombe ME, Plank T, Barth A, Asimow P, Hauri E (2020) Waterin-olivine magma ascent chronometry: every crystal is a clock. J Volcanol Geotherma Res 398:106872
- Newman S, Lowenstern JB (2002) VolatileCalc: a silicate melt–H2O–CO2 solution model written in Visual Basic for excel. Comput Geosci 28:597–604
- Nielson DL, Hulen JB (1984) Internal geology and evolution of the Redondo dome, Valles caldera, New Mexico: Journal of Geophysical Research: Solid. Earth 89:8695–8711
- Papale P, Montagna CP, Longo A (2017) Pressure evolution in shallow magma chambers upon buoyancy-driven replenishment: Geochemistry. Geophysics, Geosystems 18:1214–1224
- Phillips EH, Goff F, Kyle PR, McIntosh WC, Dunbar NW, Gardner JN (2007) The 40Ar/39Ar age constraints on the duration of resurgence at the Valles caldera, New Mexico. J Geophys Res Solid Earth 112:B8
- Rutherford MJ, Devine JD (2003) Magmatic conditions and magma ascent as indicated by hornblende phase equilibria and reactions in the 1995–2002 Soufriere Hills magma. J Petrol 44:1433–1453
- Rutherford MJ, Hill PM (1993) Magma ascent rates from amphibole breakdown: an experimental study applied to the 1980–1986 Mount St. Helens Eruptions: Journal of Geophysical Research: Solid Earth 98:19667–19685
- Savage J, Lisowski M, Prescott W, Sanford A (1980) Geodetic measurement of horizontal deformation across the Rio Grande Rift near Socorro. New Mexico: Journal of Geophysical Research: Solid Earth 85:7215–7220
- Self S, Goff F, Gardner JN, Wright JV, Kite WM (1986) Explosive rhyolitic volcanism in the Jemez Mountains: Vent locations, caldera development and relation to regional structure. J Geophy Res Solid Earth 91:1779–1798
- Skirius CM, Peterson JW, Anderson AT (1990) Homogenizing rhyolitic glass inclusions from the Bishop Tuff. Am Mineral 75:1381–1398
- Smith RL, Bailey RA (1966) The Bandelier Tuff: A study of ash-flow eruption cycles from zoned magma chambers. Bull Volcanol 29:83–103
- Stimac JA (1996) Hornblende-dacite pumice in the Tshirege member of the Bandelier Tuff: implications for magma chamber and eruptive processes. New Mexico Geological Society Fall Field Conference Guidebook 47, Jemez Mountains Region. New Mexico Geological Society, Socorro: 269-274
- Stix J, Layne GD (1996) Gas saturation and evolution of volatile and light lithophile elements in the Bandelier magma chamber between two caldera-forming eruptions. J Geophys Res Solid Earth 101:25181–25196
- Sussman AJ, Lewis CJ, Mason SN, Geissman JW, Schultz-Fellenz E, Oliva-Urcia B, Gardner J (2011) Paleomagnetism of the Quaternary Bandelier Tuff: implications for the tectonic evolution of the Española Basin Rio Grande Rift. Lithosphere 3:328–345
- Toramaru A (2006) BND (bubble number density) decompression rate meter for explosive volcanic eruptions. J Volcanol Geotherm Res 154:303–316
- Tramontano S, Gualda GA, Ghiorso MS (2017) Internal triggering of volcanic eruptions: tracking overpressure regimes for giant magma bodies. Earth Planet Sci Lett 472:142–151
- Waelkens CM (2021) Magmatic processes in a silicic caldera-forming system: Valles caldera, New Mexico, USA. Doctoral Dissertation, McGill University
- Wark D, Wolff J (2006) Mafic-recharge eruption trigger for the Bandelier and Bishop Tuffs, *in* AGU Fall Meeting Abstracts
- Wark DA, Watson EB (2006) TitaniQ: a titanium-in-quartz geothermometer. Contrib Mineral Petrol 152:743–754
- Warshaw CM, Smith RL (1988) Pyroxenes and fayalites in the Bandelier Tuff, New Mexico; temperatures and comparison with other rhyolites. Am Mineral 73:1025–1037



Bulletin of Volcanology (2022) 84:4 Page 21 of 21 4

Westgate JA, Woldegabriel G, Halls HC, Bray CJ, Barendregt RW, Pearce NJ, Sarna-Wojcicki AM, Gorton MP, Kelley RE, Schultz-Fellenz E (2019) Quaternary tephra from the Valles caldera in the volcanic field of the Jemez Mountains of New Mexico identified in western Canada. Quat Res 91:813–828

- Wolff J, Gardner J (1995) Is the Valles caldera entering a new cycle of activity? Geology 23:411–414
- Woodward LA (1977) Rate of crustal extension across the Rio Grande rift near Albuquerque. New Mex Geol 5:269–272
- Wysoczanski R, Tani K (2006) Spectroscopic FTIR imaging of water species in silicic volcanic glasses and melt inclusions: an example from the Izu-Bonin arc. J Volcanol Geotherm Res 156:302–314
- Zhang Y, Jenkins J, Xu Z (1997) Kinetics of the reaction H2O O→ 2 2OH in rhyolitic glasses upon cooling: geospeedometry and comparison with glass transition. Geochim Cosmochim Acta 61:2167–2173
- Zhang Y, Xu Z, Zhu M, Wang H (2007) Silicate melt properties and volcanic eruptions. Rev Geophys 45:RG4004

